The Astrophysical Journal, 709:644–663, 2010 February 1 doi:10.1088/0004-637X/709/2/644

GALAXY STELLAR MASS ASSEMBLY BETWEEN $0.2 < z < 2$ FROM THE S-COSMOS SURVEY*

O. Ilbert[1,2], M. Salvato[3], E. Le Floc'h[1], H. Aussel[4], P. Capak[3,5], H. J. McCracken[6], B. Mobasher[7], J. Kartaltepe[1], N. Scoville[3], D. B. Sanders[1], S. Arnouts[8], K. Bundy[9], P. Cassata[2], J.-P. Kneib[2], A. Koekemoer[10], O. Le Fèvre[2], S. Lilly[11], J. Surace[5], Y. Taniguchi[12], L. Tasca[9], D. Thompson[3,13], L. Tresse[2], M. Zamojski[3], G. Zamorani[14], and E. Zucca[14]

[1] Institute for Astronomy, 2680 Woodlawn Dr., University of Hawaii, Honolulu, HI 96822, USA
[2] Laboratoire d'Astrophysique de Marseille, Université de Provence, CNRS, BP 8, Traverse du Siphon, 13376 Marseille Cedex 12, France
[3] California Institute of Technology, MC 105-24, 1200 East California Boulevard, Pasadena, CA 91125, USA
[4] AIM Unité Mixte de Recherche CEA CNRS, Université Paris VII UMR n158, Paris, France
[5] Spitzer Science Center, California Institute of Technology, Pasadena, CA 91125, USA
[6] Institut d'Astrophysique de Paris, UMR7095 CNRS, Université Pierre et Marie Curie, 98 bis Boulevard Arago, 75014 Paris, France
[7] Department of Physics and Astronomy, University of California, Riverside, CA 92521, USA
[8] Canada France Hawaii Telescope Corporation, 65-1238 Mamalahoa Hwy, Kamuela, HI 96743, USA
[9] Department of Astronomy and Astrophysics, University of Toronto, 50 St. George Street, Room 101, Toronto, ON M58 3H4, Canada
[10] Space Telescope Science Institute, 3700 San Martin Drive, Baltimore, MD 21218, USA
[11] Department of Physics, ETH Zurich, CH-8093 Zurich, Switzerland
[12] Research Center for Space and Cosmic Evolution, Ehime University, Bunkyo-cho 2-5, Matsuyama 790-8577, Japan
[13] LBT Observatory, University of Arizona, 933 N. Cherry Ave., Tucson, AZ 85721-0065, USA
[14] INAF-Osservatorio Astronomico di Bologna, via Ranzani 1, I-40127 Bologna, Italy
Received 2009 January 6; accepted 2009 December 4; published 2010 January 6

ABSTRACT

We follow the galaxy stellar mass assembly by morphological and spectral type in the COSMOS 2 deg^2 field. We derive the stellar mass functions and stellar mass densities from $z = 2$ to $z = 0.2$ using 196,000 galaxies selected at $F_{3.6\,\mu\mathrm{m}} > 1\,\mu$Jy with accurate photometric redshifts ($\sigma_{(z_{\mathrm{phot}}-z_{\mathrm{spec}})/(1+z_{\mathrm{spec}})} = 0.008$ at $i^+ < 22.5$). Using a spectral classification, we find that $z \sim 1$ is an epoch of transition in the stellar mass assembly of quiescent galaxies. Their stellar mass density increases by 1.1 dex between $z = 1.5$–2 and $z = 0.8$–1 ($\Delta t \sim 2.5$ Gyr), but only by 0.3 dex between $z = 0.8$–1 and $z \sim 0.1$ ($\Delta t \sim 6$ Gyr). Then, we add the morphological information and find that 80%–90% of the massive quiescent galaxies ($\log \mathcal{M} \sim 11$) have an elliptical morphology at $z < 0.8$. Therefore, a dominant mechanism links the shutdown of star formation and the acquisition of an elliptical morphology in massive galaxies. Still, a significant fraction of quiescent galaxies present a Spi/Irr morphology at low mass (40%–60% at $\log \mathcal{M} \sim 9.5$), but this fraction is smaller than predicted by semi-analytical models using a "halo quenching" recipe. We also analyze the evolution of star-forming galaxies and split them into "intermediate activity" and "high activity" galaxies. We find that the most massive "high activity" galaxies end their high star formation rate phase first. Finally, the space density of massive star-forming galaxies becomes lower than the space density of massive elliptical galaxies at $z < 1$. As a consequence, the rate of "wet mergers" involved in the formation of the most massive ellipticals must decline very rapidly at $z < 1$, which could explain the observed slow down in the assembly of these quiescent and massive sources.

Key words: galaxies: evolution – galaxies: formation – galaxies: luminosity function, mass function

Online-only material: color figures

1. INTRODUCTION

A clear and comprehensive picture describing the physical processes that regulate stellar mass growth in galaxies is still missing in our understanding of galaxy evolution. Indeed, the stellar mass growth is regulated by a complex interplay between the radiative cooling of the gas (e.g., White & Rees 1978), cold accretion (e.g., Kereš et al. 2005), the spatial redistribution of the gas along the hierarchical growth of dark matter halos (e.g., Springel et al. 2006), and the feedback from supernovae and active galactic nuclei (AGNs; e.g., Benson et al. 2003; Croton et al. 2006). AGN feedback is a central process recently added to galaxy formation models in order to suppress excessive cooling of the gas in massive halos (e.g., Bower et al. 2006; Croton et al. 2006; Menci et al. 2006; Cattaneo et al. 2006). Even with the inclusion of AGN feedback, semi-analytical models still miss a population of massive galaxies at $z \sim 2$ (McCracken et al. 2010) and overproduce the number density of low-mass galaxies (e.g., Kitzbichler & White 2007; Stringer et al. 2009). Therefore, a better description of star formation activity is still needed. The stellar mass function (MF), as studied in this paper, characterizes how star formation activity build the stellar mass of each galaxy type.

Merging between galaxies is another central mechanism in stellar mass assembly. However, there appears to be little consensus between direct estimates of the merger rate (e.g., Le

* Based on observations with the NASA/ESA *Hubble Space Telescope*, obtained at the Space Telescope Science Institute, which is operated by AURA Inc., under NASA contract NAS 5-26555. Also based on observations made with the *Spitzer Space Telescope*, which is operated by the Jet Propulsion Laboratory, California Institute of Technology, under NASA contract 1407. Also based on data collected at: the Subaru Telescope, which is operated by the National Astronomical Observatory of Japan; the *XMM-Newton*, an ESA science mission with instruments and contributions directly funded by ESA Member States and NASA; the European Southern Observatory under Large Program 175.A-0839, Chile; Kitt Peak National Observatory, Cerro Tololo Inter-American Observatory, and the National Optical Astronomy Observatory, which are operated by the Association of Universities for Research in Astronomy, Inc. (AURA) under cooperative agreement with the National Science Foundation; and the Canada–France–Hawaii Telescope with MegaPrime/MegaCam operated as a joint project by the CFHT Corporation, CEA/DAPNIA, the NRC and CADC of Canada, the CNRS of France, TERAPIX, and the University of Hawaii.

Fèvre et al. 2000; Kartaltepe et al. 2007; Lotz et al. 2008). An alternative approach is to study the product of major mergers. Indeed, these are expected to deplete the low mass end of the MF in favor of high-mass galaxies, and to produce galaxies with elliptical morphologies (e.g., Toomre & Toomre 1972). Therefore, a detailed measurement of the MF by galaxy type can yield valuable clues on galaxy assembly by mergers. This measurement can also be considered as a crucial test of the hierarchical paradigm since the assembly of elliptical galaxies is expected to follow a hierarchical buildup similar to that of their host dark matter halos (e.g., Kauffmann et al. 1993; de Lucia et al. 2006).

Following the stellar mass assembly of a given galaxy population requires that the sample be split into well-characterized galaxy types. A multi-color classification scheme is often the only possible method to split the faint high redshift samples by type. The bimodal distribution of the galaxies in a color–magnitude diagram is a common tool often used to differentiate two populations: "blue cloud" and "red sequence" galaxies (e.g., Bell et al. 2004; Faber et al. 2007; Franzetti et al. 2007). The red sequence galaxies include mostly passive galaxies with an elliptical morphology (e.g., Strateva et al. 2001; Cassata et al. 2007), but also a significant fraction of dust-extincted star-forming galaxies (e.g., Williams et al. 2009) and Spi/Irr galaxies with a quenched star formation (e.g., Bell 2008). A novel color–color selection technique ($M_U - M_V$ versus $M_V - M_J$) has been proposed by Williams et al. (2009). This color–color selection breaks the degeneracies between dust-extincted star-forming galaxies and those with quenched star formation. This diagram is more efficient for detecting a bimodal distribution than a color–magnitude plot (Williams et al. 2009). An alternative multi-color classification method is based on a template-fitting procedure (e.g., Lin et al. 1999; Wolf et al. 2003; Zucca et al. 2006). The advantage of this method is that it defines more than two spectral types. But the different template selections are difficult to compare from one study to another.

However, the spectral classifications are sensitive to the instantaneous star formation rate (SFR). Different galaxy populations mixed in the same spectral class can be disentangled by adding morphological information. Automatic morphological classifications (e.g., Abraham et al. 1996) performed on high resolution images are efficient for discriminating at least two robust classes: E/S0 and Spi/Irr galaxies (e.g., Lauger et al. 2005; Menanteau et al. 2006; Lotz et al. 2008; Capak et al. 2007). The combination of morphological and spectral classifications allow us to isolate the "blue elliptical" galaxies (e.g., Cross et al. 2004; Menanteau et al. 2006; Ilbert et al. 2006a) which could include newly formed ellipticals still harboring star formation (e.g., Van Dokkum & Franx 2001), Spi/Irr with quenched star formation (Bell 2008), and passive elliptical galaxies (e.g., Abraham et al. 2007).

Stellar mass assembly in galaxies by spectral and morphological type has already been investigated using deep optical and near-infrared (NIR) surveys. Bundy et al. (2005), Franceschini et al. (2006), and Pannella et al. (2006) have derived the MF by morphological type using respectively 2150, 1478, and 1645 galaxies at $z < 1.4$ in the two GOODS fields covering 160 arcmin^2 each (Giavalisco et al. 2004). Borch et al. (2006) and Bundy et al. (2006) derived the MF for blue cloud and red sequence galaxies using larger fields of 0.8 deg^2 and 1.5 deg^2, respectively. These analyses showed that massive elliptical or red sequence galaxies are already in place at $z \sim 1$, while the density is still increasing at lower masses. Vergani et al. (2008) confirmed these results using the 4000 Å Balmer break to separate galaxy populations in early- and late-type systems. Therefore, the "downsizing" pattern found by Cowie et al. (1996) could be extended to the assembly process of ellipticals at $z < 1$ (e.g., Cimatti et al. 2006). Using the *K*-band luminosity function rather than the MF, Arnouts et al. (2007) and Cirasuolo et al. (2007) were able to study the stellar mass assembly for red sequence and blue cloud galaxies at $z > 1$. They found a rapid rise in the space density of massive red sequence galaxies from $z \sim 2$ to $z \sim 1$ (Cirasuolo et al. 2007 and Arnouts et al. 2007). Abraham et al. (2007) combined morphology and colors to study stellar mass evolution for 144 galaxies with spectroscopic redshifts at $z > 0.8$ using data from the Gemini Deep Deep Survey. They confirmed the importance of this redshift range in the birth of passive elliptical galaxies.

This paper presents the evolution of the galaxy stellar MF and stellar mass density using the COSMOS survey. This survey (Scoville et al. 2007) provides four main advantages over previous studies that have attempted to measure MF evolution: (1) it covers 2 deg^2 which reduces the effect of cosmic variance; (2) a morphological classification can be carried out based on the *Hubble Space Telescope*/Advanced Camera for Surveys (*HST*/ACS) images (Koekemoer et al. 2007); (3) deep *Spitzer*/IRAC (3.6–8.0 μm; Sanders et al. 2007) and Canada–France–Hawaii Telescope (CFHT)/WIRCAM K_s-band data (McCracken et al. 2010) allow us to estimate accurate stellar masses out to $z \sim 2$; and (4) the extensive multi-λ coverage of COSMOS provides accurate photometric redshifts (Ilbert et al. 2009) that can be used to derive the galaxy stellar MF. We took special care to characterize the galaxy populations, including galaxy morphologies. A first study by Scarlata et al. (2007) in the COSMOS field already combined morphological and spectral classifications to study the *B*-band luminosity function. We supplement this study by deriving the stellar MF. We provide an estimate of the MF which simultaneously covers a large range of redshift ($0.2 < z < 2$) and a large range of stellar masses ($10^9 < \mathcal{M}/\mathcal{M}_\odot < 10^{12}$) using *K*-band images that are 1.5 mag deeper than those used by Bundy et al. (2006). We also combine morphological and spectral classifications over a field 20× and 100× larger than Bundy et al. (2005) and Abraham et al. (2007), respectively.

The COSMOS data are introduced in Section 2. The criteria used to split the galaxy sample into various populations are described in Section 3. We present the method used to compute the galaxy stellar masses in Section 4. Sections 5–8 present the stellar MF and stellar mass density of total, early- and late-type samples, respectively. The results are discussed in Section 9. Throughout this paper, we use the standard cosmology ($\Omega_m = 0.3$, $\Omega_\Lambda = 0.7$) with $H_0 = 70$ km s^{-1} Mpc^{-1}. Magnitudes are given in the AB system. The stellar masses are given in units of solar masses ($\mathcal{M}_\odot$) for a Chabrier initial mass function (hereafter IMF). The stellar masses based on a Salpeter IMF (Arnouts et al. 2007), "diet" Salpeter IMF (Bell 2008), and Kroupa IMF (Borch et al. 2006) were converted into a Chabrier IMF by adding −0.24 dex, −0.09 dex, and 0 dex, respectively, to the logarithm of the stellar masses.

2. DATA

2.1. The 3.6 μm Selected Catalog

This analysis is based on a mass selected sample as generated from the 3.6 μm IRAC catalog of the S-COSMOS survey (Sanders et al. 2007).

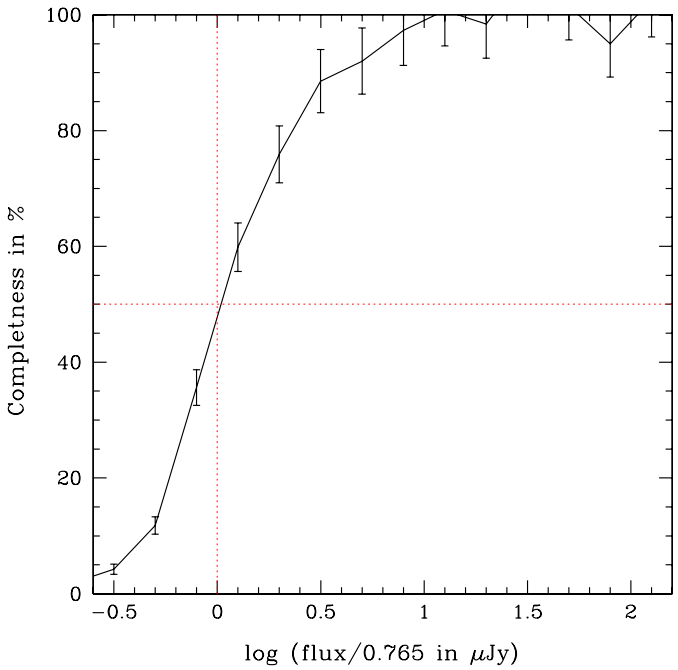

Figure 1. Completeness at 3.6 μm: fraction of sources simulated in the 3.6 μm image which are detected with SExtractor, as a function of flux.

(A color version of this figure is available in the online journal.)

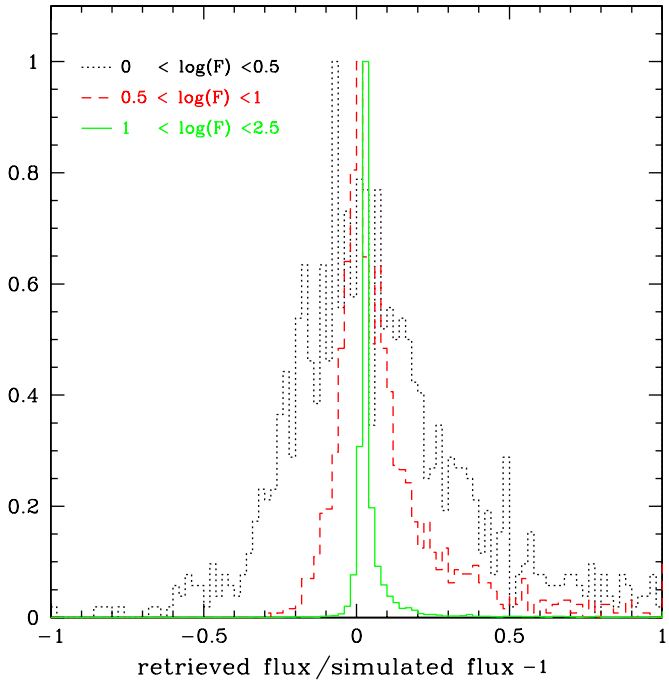

Figure 2. Ratio between the 3.6 μm flux measured with SExtractor over the simulated flux.

(A color version of this figure is available in the online journal.)

The IRAC data were taken during the *Spitzer* Cycle 2 S-COSMOS survey, which used 166 hr to map the full 2 deg^2 COSMOS field (centered at J2000 R.A. = 10:00:28.6, decl. = +02:12:21.0). The observations were carried out in four channels: 3.6 μm, 4.5 μm, 5.6 μm, and 8.0 μm. The data were initially processed by the Spitzer Science Center (SSC). The raw scientific exposures were flux calibrated and corrected for well-understood instrumental signatures using a pipeline described by Surace et al. (2005). Once the frame-level images were prepared, they were projected onto a common tangent projection and co-added using the SSC MOPEX software.[15] The images and the corresponding uncertainty maps were generated for each of the four channels.

The source catalog was extracted using the SExtractor software (Bertin & Arnouts 1996). The source detection is performed at 3.6 μm. The IRAC 3.6 μm images have a point-spread function (PSF) of 1.″7 which necessitates a careful deblending of the sources. This was obtained with a Mexican Hat filtering of the images by SExtractor. In order to estimate the completeness of the 3.6 μm catalog, we simulated point-like sources in the 3.6 μm mosaic. We simulated simultaneously 10,000 sources with a flux ranging from 0.1 to 300 μJy. The simulated sources were distributed randomly in the field without any a priori knowledge of the position of the real 3.6 μm sources (these sources can fall behind or nearby a real bright source). We run SExtractor on this new image using exactly the same configuration as for real data. Finally, we estimated the fraction of simulated sources that we are able to detect, as a function of flux (see Figure 1). We found that the IRAC catalog is 90% complete at 5 μJy and 50% complete at 1 μJy.

We also used the SExtractor software the measure the IRAC fluxes. Following Surace et al. (2005), the fluxes were measured over a circular aperture of radius 1.″9. This small radius provides a flux measurement less affected by the presence of nearby sources. We tested the accuracy of the fluxes recovered by SExtractor using the simulation described previously. Figure 2 shows the comparison between the simulated flux and the flux measured by SExtractor. We obtained a flux accuracy of 5%, 10%, and 25% for sources at 10 μJy $< F <$ 300 μJy, 3 μJy $< F <$ 10 μJy, and 1 μJy $< F <$ 3 μJy, respectively. These uncertainties on the 3.6 μm fluxes are not directly propagated into the stellar masses since deep near-infrared data (J, H, K) as well as 24 optical bands constrain the rescaling of the best-fit templates. Based on the same simulation, we derived an aperture correction of 1.31 at 3.6 μm to convert the aperture flux to total flux (assuming the sources to be point-like). However, we caution the reader that specific software like CONVPHOT (De Santis et al. 2007) or TFIT (Laidler et al. 2007) could provide flux measurements less affected by the confusion by using the K-band image as a prior.

Finally, we masked the brightest sources ($K_s < 12$), as well as poor image quality areas and the field boundaries. After removing the masked areas, the 3.6 μm catalog contains a total of 306,000 sources brighter than 1 μJy (50% completeness limit) over an area of 2.3 deg^2.

2.2. Optical and Photo-z Catalogs

We cross-matched the 3.6 μm catalog with the COSMOS photometric (P. Capak et al. 2010, in preparation) and photo-z catalogs (Ilbert et al. 2009). The photo-z were derived for all of the sources in the COSMOS photometric catalog (1,500,515 sources in total, and 937,013 sources at $i^+ <$ 26.5). The photometric fluxes are measured in 31 bands (2 bands from the *Galaxy Evolution Explorer* (*GALEX*), 6 broad bands from the SuprimeCam/Subaru camera, 2 broad bands from MEGACAM at CFHT, 14 medium and narrow bands from SuprimeCam/Subaru, J band from the WFCAM/UKIRT camera, H- and K band from the WIRCAM/CFHT camera, and

[15] http://ssc.spitzer.caltech.edu/postbcd/

the 4 IRAC/*Spitzer* channels). The imaging data are extremely deep, reaching $u^* \sim 27$, $i^+ \sim 26.2$, and $K_s \sim 23.7$ for a 5σ detection in a $3''$ aperture (the sensitivities are listed in Capak et al. 2007 and Salvato et al. 2009). We restricted this study to the area covered by the deep optical Subaru image (2 deg^2, $149.4114 < \alpha < 150.8269$ and $1.4987 < \delta < 2.9127$) in order to assure a robust photo-z estimate.

We derived photometric redshifts using the *Le Phare*[16] code (Arnouts et al. 2002 and Ilbert et al. 2006b) with a χ^2 template-fitting method. The photo-z have been updated in comparison to Ilbert et al. (2009) by including new H-band data. The photo-z are estimated using the median of the probability distribution function (PDFz) rather than the minimum of the χ^2 distribution. The photo-z were calibrated with 4148 spectroscopic redshifts at $i^+_{\rm AB} < 22.5$ from the zCOSMOS survey (S. Lilly et al. 2010, in preparation). The comparison between the photometric and spectroscopic redshifts shows that the fraction of outliers (defined as galaxies with $(z_{\rm phot} - z_{\rm spec})/(1 + z_{\rm spec}) > 0.15$) is less than 1% and the accuracy is as good as $\sigma_{(z_{\rm phot}-z_{\rm spec})/(1+z_{\rm spec})} = 0.008$ at $i^+_{\rm AB} < 22.5$. A spectroscopic follow-up of 24 μm selected sources at $z < 1.5$ (J. S. Kartaltepe et al. 2010, in preparation) allows us to characterize the photo-z accuracy at fainter magnitude. We found $\sigma_{(z_{\rm phot}-z_{\rm spec})/(1+z_{\rm spec})} = 0.011$ at $22.5 < i^+_{\rm AB} < 24$ and $\sigma_{(z_{\rm phot}-z_{\rm spec})/(1+z_{\rm spec})} = 0.053$ at $24 < i^+_{\rm AB} < 25$ for this infrared selected sample. At $z > 1.5$, we used the zCOSMOS-faint spectroscopic sample (S. Lilly et al. 2010, in preparation) to quantify the quality of the photo-z in the magnitude/redshift range where the photo-z are expected to have the highest uncertainty. These color selected galaxies have median apparent magnitude of $i^+_{\rm med} \sim 24.1$ and a median redshift of 2.1. At $1.5 < z < 3$, we obtained an accuracy of $\sigma_{\Delta z/(1+z)} = 0.04$ with 10% of catastrophic failures. However, these various spec-z samples probe only specific populations (infrared selected, color selected). Figure 8 of Ilbert et al. (2009) shows that the photo-z 1σ error derived from the PDFz is well representative of the photo-z accuracy. The median 1σ error is 0.02 for the full catalog at $F_{3.6\,\mu{\rm m}} > 1\,\mu$Jy and 0.08 in the redshift range $1.25 < z < 2$. We also showed in Figure 12 of Ilbert et al. (2009) that the photo-z accuracy is degraded at $i^+_{\rm AB} > 25.5$. Therefore, we take special care in limiting the contribution of these faint sources in our analysis (see Section 4.4).

2.3. Identification of the 3.6 μm Source Counterparts

We cross-matched the 3.6 μm and photo-z catalogs by taking the closest counterpart within a radius of $1''$. The distances of the first and second closest optical counterpart have a median value of $0\farcs2$ and $2\farcs5$, respectively. The two distributions intersect at $1''$. Therefore, we adopted a matching distance of $1''$ which is a good compromise to detect the maximum of optical counterparts and limits the risk of wrong identification. Still, 2.6% of the IRAC sources have two possible optical counterparts in less than $1''$. In order to estimate the probability of having identified the wrong optical counterpart, we multiplied the probability of having the right counterpart by the probability of having another optical source at a lower distance (using the distance distributions of the first and second closest counterpart, respectively). We obtained that the probability of having identified the wrong optical counterpart is 0.1%. We found a similar probability of 0.4% using simulations.

We identified 8507 3.6 μm sources without optical counterpart (about 4% of the IRAC catalog). Most of these sources are extremely faint at 3.6 μm, without counterpart in the K-band selected catalog (McCracken et al. 2010). This sample includes also a significant fraction of fake detections created by the residual of the muxbleed correction (Surace et al. 2005). Still, we were able to identify 2714 IRAC sources which are clearly non-detected in optical and are detected in the K-band selected catalog. These sources can be $z > 1.5$ quiescent systems. Therefore, we included them in our analysis. We measured a photo-z for these sources using NIR and IRAC data. An upper limit was set in i^+ since this band was used for galaxy detection in P. Capak et al. (2010, in preparation). The averaged redshift of this population is $z \sim 2.9$. 93% and 77% of these sources are at $z > 1.5$ and $z > 2$, respectively. In any case, the impact of this galaxy population on our analysis is low since the stellar mass limits are set to ensure a low fraction of sources with $i^+_{\rm AB} > 25.5$ in the stellar mass sample (see Section 4.4).

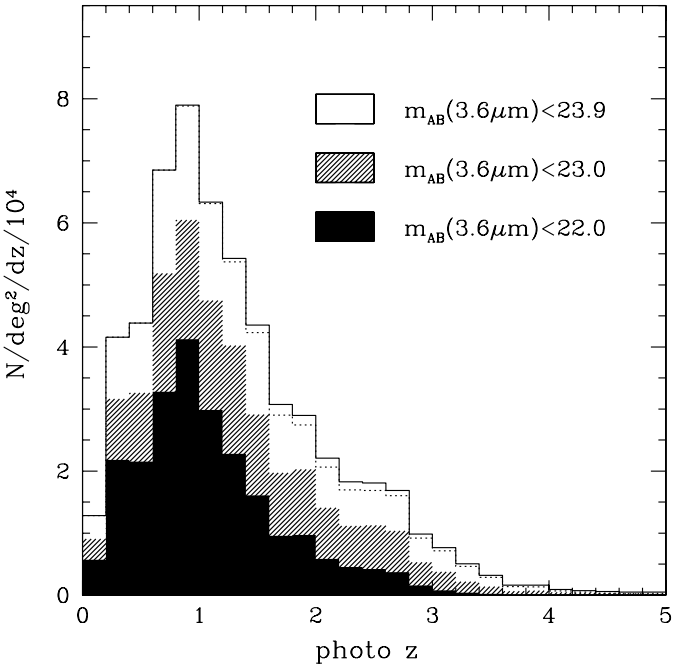

Figure 3. Photometric redshift distributions for the 3.6 μm selected sample ($m_{\rm AB}(3.6\,\mu{\rm m}) = -2.5\log F + 23.9$ where F is the flux in μJy). The dotted line corresponds to the redshift distribution without the galaxies not detected in optical.

Finally, we removed all of the sources flagged as star or AGN. Stars were removed from the sample by comparing the χ^2 evaluated for both the galaxy templates and stellar templates (see Section 3.6 of Ilbert et al. 2009). The 1887 sources (1% of the total sample) detected with *XMM-Newton*–COSMOS (Hasinger et al. 2007; Brusa et al. 2007; Salvato et al. 2009) were removed from the sample since their optical emissivity is likely dominated by an AGN.

To summarize, this study is based on the S-COSMOS 3.6 μm selected catalog which is 50% complete at 1 μJy. We cross-match this catalog with the full optical and photo-z catalog using a match distance of $1''$. The photo-z accuracy is as good as $\sigma_{(z_{\rm phot}-z_{\rm spec})/(1+z_{\rm spec})} = 0.008$ at $i^+_{\rm AB} < 22.5$. The final sample (after having removed the stars, the *XMM-Newton* sources, the masked areas, and the objects without optical counterparts) contains 196,000 galaxies at $F_{3.6\,\mu{\rm m}} > 1\,\mu$Jy over an effective area of 1.73 deg^2. Figure 3 shows the redshift distributions for the $F_{3.6\,\mu{\rm m}} > 1\,\mu$Jy selected sample with a median redshift of $z \sim 1.1$.

[16] http://www.cfht.hawaii.edu/~arnouts/LEPHARE/cfht_lephare

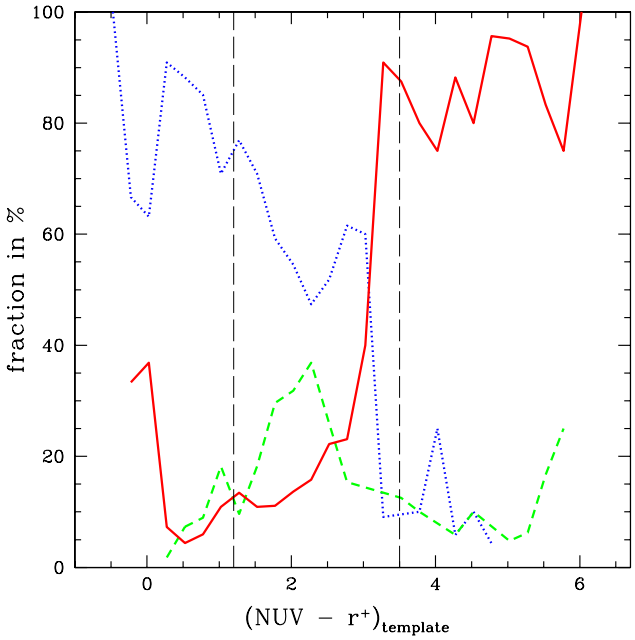

Figure 4. Distribution of the unextincted rest-frame color $(\mathrm{NUV}-r^+)_{\mathrm{template}}$ of 1500 visually classified galaxies (late spiral and irregular: blue dotted line; early spiral: green dashed line; E/S0: red solid line). The vertical dashed lines show the separation between the "quiescent," "intermediate activity," and "high activity" galaxies.

(A color version of this figure is available in the online journal.)

3. MORPHOLOGICAL AND SPECTRAL GALAXY CLASSIFICATIONS

In this paper, we study the galaxy stellar MFs per morphological and spectral type. This section presents the criteria used to define the various galaxy types: E/S0 and Spi/Irr galaxies based on their morphology; three spectral classes ("quiescent," "intermediate activity," and "high activity" galaxies) using best-fit templates.

3.1. Morphological Classification

We used the high resolution *HST*/ACS images (Koekemoer et al. 2007) to perform a morphological classification of our galaxy sample. The images in the F814W filter reach a depth of 27.8 mag for a point source at 5σ. We adopted two independent morphological classifications to separate E/S0 and Spi/Irr galaxies.

The first classification is based on the Gini (G) and concentration (C) parameters measured by Abraham et al. (2007) (hereafter G–C classification). The Gini parameter measures the inequality with which the light of a galaxy is distributed among its constituent pixels. Like Capak et al. (2007), the galaxies with $G > 0.43$ were considered E/S0 galaxies. In addition, we rejected from the E/S0 sample the galaxies with a concentration parameter smaller than 0.3 (Ilbert et al. 2006a).

The second classification was performed by P. Cassata et al. (2010, in preparation; hereafter C09 classification). The structural parameters are measured using a "quasi-Petrosian" image thresholding technique (Abraham et al. 2007). This classification includes Gini, Concentration, Asymmetry, and M20 (e.g., Lotz et al. 2004). The multi-dimensional parameter space is automatically converted into an E/S0 and Spi/Irr classification by matching these parameters with those of a training sample of 250 visually classified galaxies (50 galaxies per 0.5 mag bin out to $i^+_{\mathrm{AB}} < 24$).

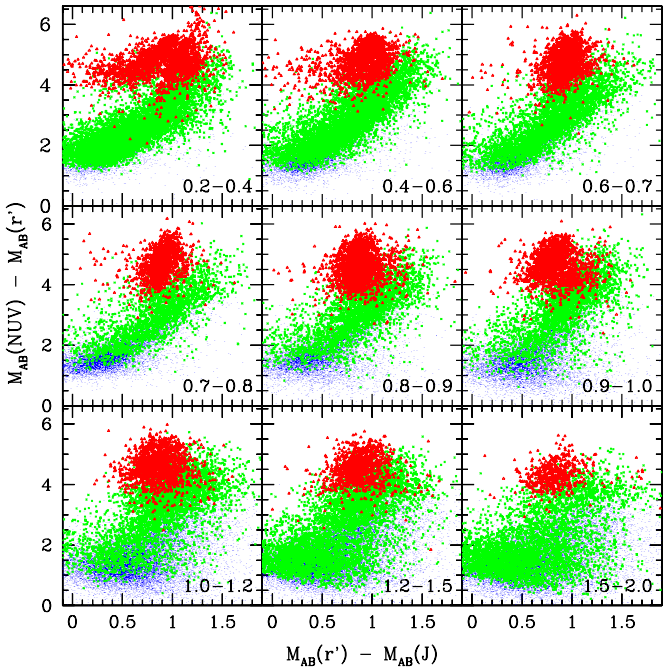

Figure 5. Rest-frame colors $M(\mathrm{NUV})-M(r^+)$ vs. $M(r^+)-M(J)$ (not corrected for dust reddening) from $z = 0.2$ (top left panel) to $z = 2$ (bottom right panel). The red open triangles, green crosses, and blue points are the galaxies selected as "quiescent," "intermediate activity," and "high activity," respectively, on the basis of their unextincted rest-frame color $(\mathrm{NUV}-r^+)_{\mathrm{template}}$.

(A color version of this figure is available in the online journal.)

The E/S0 selection performed by C09 is more conservative than the G–C classification (i.e., less contaminated by spiral galaxies), but is likely to be more incomplete. Indeed, less than 1% of the E/S0 sources from C09 are not identified as E/S0 with the G–C parameters, while 33% of the E/S0 sources identified with the G–C parameters are not identified by C09 (at $\log \mathcal{M} > 10$ and $z < 1.2$).

3.2. Spectral Classification

A set of spectral energy distribution (SED) templates was generated using the Bruzual & Charlot (2003; BC03) package and fitted to the multi-color data (see Section 4.1). The extinction is added as a free parameter in the fit. We used the unextincted rest-frame colors $(\mathrm{NUV}-r^+)_{\mathrm{template}}$ of the templates to define three spectral classes: (1) the "quiescent" galaxies with $(\mathrm{NUV}-r^+)_{\mathrm{template}} > 3.5$; (2) the "intermediate activity" galaxies with $1.2 < (\mathrm{NUV}-r^+)_{\mathrm{template}} < 3.5$; (3) the "high activity" galaxies with $(\mathrm{NUV}-r^+)_{\mathrm{template}} < 1.2$.

Figure 4 shows the $(\mathrm{NUV}-r^+)_{\mathrm{template}}$ distribution of a sample of 1500 galaxies that we visually classified as E/S0, early spiral, late spiral, or irregular. The 1500 galaxies were selected to provide an unambiguous visual classification (isolated and bright galaxies) but were not selected to be statistically representative of the 3.6 μm sample. A cut at $(\mathrm{NUV}-r^+)_{\mathrm{template}} > 3.5$ isolates well the E/S0 galaxies. The "intermediate activity" class ($1.2 < (\mathrm{NUV}-r^+)_{\mathrm{template}} < 3.5$) includes most of the visually selected early spiral galaxies but is strongly contaminated by late spiral and irregular galaxies.

Figure 5 shows a slightly modified version of the color–color selection technique ($M_U - M_V$ versus $M_V - M_J$) proposed by Williams et al. (2009). We used the color NUV $- r^+$ instead of $U - V$ since this color is a better indicator of the current versus past star formation activity (e.g., Martin et al. 2007; Arnouts et al. 2007). The rest-frame colors were computed as described

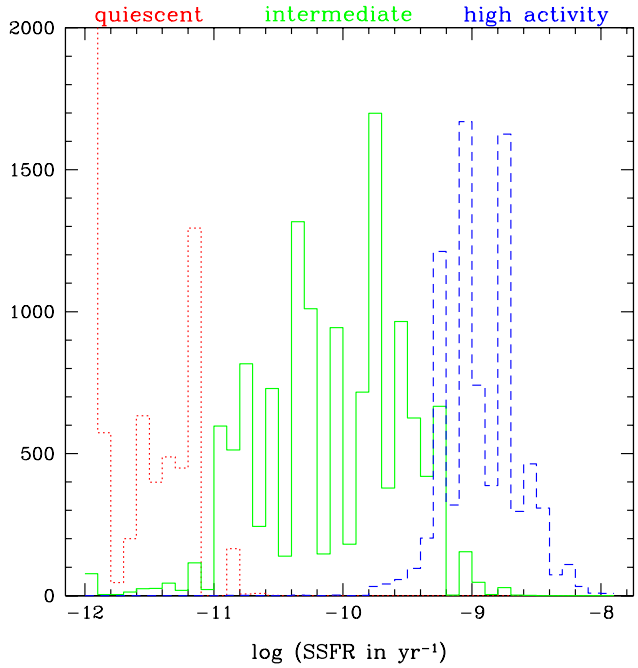

Figure 6. Distribution of the Specific SFR (SSFR) for the "quiescent" (red dotted line), "intermediate activity" (green solid line), and "high activity" (blue dashed line) galaxies (at $0.2 < z < 1.2$ and $\log \mathcal{M} > 10$; see Section 3.2).
(A color version of this figure is available in the online journal.)

in Appendix A and are not corrected for internal dust attenuation (by contrast with $(\mathrm{NUV} - r^+)_{\mathrm{template}}$ which is corrected for dust attenuation). A red clump appears clearly from $z = 0.2$ out to $z = 2$. This clump is mostly composed of "quiescent" galaxies. Therefore, our "quiescent" population is similar to the red clump population selected by Williams et al. (2009). The galaxies with a red $\mathrm{NUV} - r^+ > 4.5$ rest-frame color are well separated into a "quiescent" population with $\mathrm{r}^+ - J < 1.2$ (red clump) and a dust-extincted star-forming population with $\mathrm{r}^+ - J > 1.2$.

Finally, we show in Figure 6 that each spectral class corresponds to a range of Specific SFR (SSFR), computed as the instantaneous SFR from the best-fit template divided by the stellar mass.

To summarize, we used the *HST*/ACS images to separate E/S0 and Spi/Irr galaxies using two morphological classification methods (C09 and G–C). We also defined three spectral classes on the basis of the best-fit templates which are "quiescent," "intermediate activity," and "high activity" galaxies. These three spectral classes are well separated in ranges of SSFR. We showed that our "quiescent" population matches well with the red clump galaxies found by Williams et al. (2009) and is consistent with an E/S0 population selected morphologically.

4. THE GALAXY STELLAR MASS SAMPLE

In this section, we describe the method used to measure galaxy stellar masses and the galaxy stellar MF.

4.1. Technique Used for Estimating Stellar Masses

We used stellar population synthesis (SPS) models to convert luminosity into stellar mass (e.g., Bell et al. 2003; Fontana et al. 2004). The stellar mass is the factor needed to rescale the best-fit template (normalized at one solar mass) for the intrinsic luminosities. The SED templates were generated with the SPS package developed by BC03. We assumed an universal IMF from Chabrier (2003) and an exponentially declining star formation history $\mathrm{SFR} \propto e^{-t/\tau}$ (τ in the range 0.1 Gyr–30 Gyr). The SEDs were generated for a grid of 51 ages (in the range 0.1 Gyr–14.5 Gyr). Dust extinction was applied to the templates using the Calzetti et al. (2000) law ($E(B-V)$ in the range 0–0.5). We used models with two different metallicities. The parameters used to generate the SED templates are listed in Table 1. Following Fontana et al. (2006) and Pozzetti et al. (2007), we imposed the prior $E(B - V) < 0.15$ if $\mathrm{age}/\tau > 4$ (a significant extinction is only allowed for galaxies with a high SFR).

Table 1
Parameters Used to Generate the SED Templates with the BC03 Package

τ (Gyr)	$E(B-V)$	z
0.1	0	0.02 ($Z_\odot$)
0.3	0.1	0.008
1	0.2	
2	0.3	
3	0.4	
5	0.5	
10		
15		
30		

We introduced the fluxes measured at 24 μm with the *Spitzer*/MIPS instrument (H. Aussel et al. 2010, in preparation) as a constraint in the template-fitting procedure, as detailed in Appendix B; however, the 24 μm constraint had little effect on the derived stellar masses. The dispersion between the stellar masses with and without using this constraint is 0.014 dex, and only 1% of the sample differs by more than 0.2 dex.

All the available bands were used to compute the stellar masses (broad bands as well as medium bands). The IRAC data were included in the fit. We compared the stellar masses computed with and without IRAC. We obtained a dispersion of 0.02, 0.02, 0.04, 0.11 dex at $z = 0.2$–0.5, $z = 0.5$–1, $z = 1$–1.5, $z = 1.5$–2, respectively. At $z < 1.5$, the IRAC data have a small impact on the stellar masses, negligible in comparison to the 0.2 dex uncertainty expected in the stellar mass estimate (e.g., Pozzetti et al. 2007; Longhetti & Saracco 2008). At $z > 1.5$, including the IRAC data modifies significantly the stellar masses. The IRAC data are necessary since the K band does not probe anymore the NIR rest-frame wavelength range.

4.2. Systematic Uncertainties in the Stellar Mass Estimate

We quantified how the stellar mass accuracy is affected by the use of photo-z rather than spectro-z. Figure 7 shows the difference between the stellar masses computed with the photometric and spectroscopic redshifts. We used two spectroscopic samples: the zCOSMOS bright spectroscopic sample selected at $i^+_{\mathrm{AB}} < 22.5$ (S. Lilly et al. 2010, in preparation) and a spectroscopic follow-up of 24 μm selected sources (median flux $F_{24\,\mu\mathrm{m}} \sim 140\,\mu$Jy) by J. S. Kartaltepe et al. (2010, in preparation). The infrared follow-up supplements very well the zCOSMOS spectro-z since the former sample is fainter ($18 < i^+_{\mathrm{AB}} < 25$ with 43% of the sources being fainter than $i^+_{\mathrm{AB}} = 22.5$) and extends out to $z \sim 1.5$ (median redshift of $z \sim 0.74$). We found a median difference smaller than 0.002 dex between the photo-z and the spectro-z stellar masses for both samples. Therefore, no systematic offsets appear to be introduced by the use of our photo-z. The dispersion between the two estimates is smaller than $\sim$0.03 dex. This dispersion is 10$\times$ smaller than the

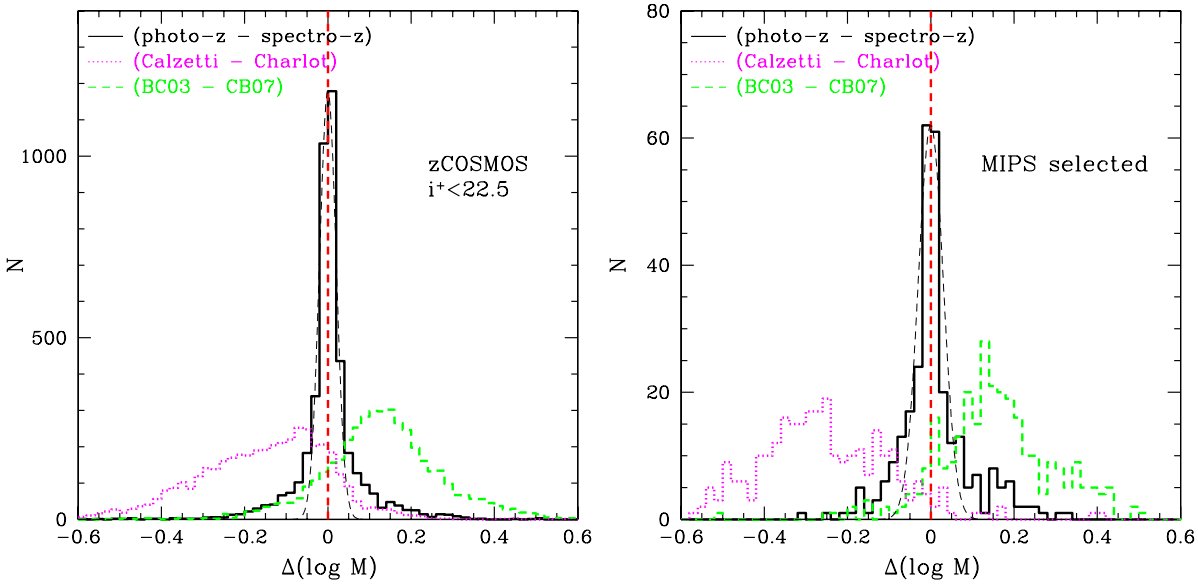

Figure 7. Black solid line histograms show the difference between the stellar masses computed with photo-z and spectro-z. We used the zCOSMOS spectroscopic sample selected at $i^+_{\rm AB} < 22.5$ (S. Lilly et al. 2010, in preparation) in the left panel and the spectro-z of infrared selected sources from J. S. Kartaltepe et al. (2010, in preparation) in the right panel. The thin black dashed lines are Gaussian distributions with $\sigma = 0.02$ (left panel) and $\sigma = 0.03$ (right panel). The green dashed lines show the difference between the stellar masses computed with BC03 and S. Charlot & A. G. Bruzual (2007, private communication). The magenta dotted lines show the differences between the stellar masses computed using the Calzetti et al. (2000) and Charlot & Fall (2000) extinction laws. The redshifts were set to the spectro-z values in the two last cases. Systematic uncertainties due to the models dominate the errors introduced by the photo-z, at least in the magnitude/redshift range explored with our spectroscopic samples.

(A color version of this figure is available in the online journal.)

systematic uncertainties expected in the stellar mass estimate (e.g., Pozzetti et al. 2007; Longhetti & Saracco 2008), at least in the magnitude/redshift space covered by the spectroscopic samples.

The choice of extinction law impacts the fit of the template and therefore the mass-to-light ratio. We computed the stellar masses using both the Calzetti et al. (2000) and the Charlot & Fall (2000) extinction laws (the latter is included in BC03). The redshifts are set to the spectro-z values. The median difference between the two stellar mass estimates (Calzetti – Charlot & Fall) is −0.14 dex with a dispersion of 0.10 dex for the zCOSMOS sample (left panel of Figure 7). This median difference reaches −0.27 dex for the MIPS spectroscopic sample, showing that the systematic offset is larger for massive galaxies with a high SFR. We adopted the Calzetti et al. (2000) extinction law. This choice is favored by a comparison between the SFR derived from the best-fit template and the SFR measured from mid-infrared 24 μm data, as described in Appendix B.

The stellar mass estimate depends also on the assumed SPS model. We computed the stellar masses with an upgraded version of the BC03 model including a better treatment of the thermally pulsing asymptotic giant branch (TP-AGB) phase (Bruzual 2007; S. Charlot & A. G. Bruzual 2007, private communication). Figure 7 shows a comparison of the stellar mass estimates using the two versions of the models. We find a median difference of 0.13–0.15 dex and a dispersion of 0.09 dex. Pozzetti et al. (2007) measured a difference of 0.14 dex between the stellar masses computed with the BC03 and the Maraston (2005) models (which also includes treatment of the TP-AGB stars), in agreement with our results. We used the public version of BC03 for consistency with results from the literature. However, the MF computed in this paper have also been computed with the upgraded version of BC03, and our conclusions remained unchanged.

4.3. Method to Estimate the MF

We measured the stellar MFs using the tool ALF (Algorithm for Luminosity Function; Ilbert et al. 2005). This tool includes the STY parametric estimator (Sandage et al. 1979) and three non-parametric estimators: the $1/V_{\rm max}$ (Schmidt 1968), C^+ (Lynden-Bell 1971 and Zucca et al. 1997), and the Step-Wise Maximum Likelihood (SWML; Efstathiou et al. 1988). A brief introduction of these standard estimators is given in Appendix C.

We weighted each galaxy according to the completeness of the 3.6 μm catalog (see Section 2.1 and Figure 1). We attributed a weight to each source depending on the 3.6 μm flux. This weight is the inverse fraction of 3.6 μm sources detected at this flux (e.g., a weight of 2 is given to the sources at $F_{3.6\,\mu{\rm m}} \sim 1\,\mu$Jy).

We also performed extensive simulations in order to propagate the photo-z uncertainties into the MF. A redshift PDFz was attributed to each galaxy when we measured the photo-z (see Ilbert et al. 2009). We created 20 catalogs by randomly picking a redshift within the PDFz of each object. The MFs were measured for each of the 20 catalogs in every redshift bin and for each galaxy population. Finally, the dispersion of the Schechter parameters was measured over the 20 realizations. We added in quadrature the Poissonian errors and these errors induced by the use of photo-z.

4.4. Considered Stellar Mass Range for the MF Estimate

The low mass limits considered for the MF estimates are set in order to insure a complete and unbiased stellar mass sample with accurate photo-z.

We defined the low stellar mass limits in order to reduce the fraction of optically faint sources with low quality photo-z in the stellar mass sample. Figure 8 shows the fraction of galaxies with $i^+ > 25.5$ (dashed lines) as a function of the stellar mass. We

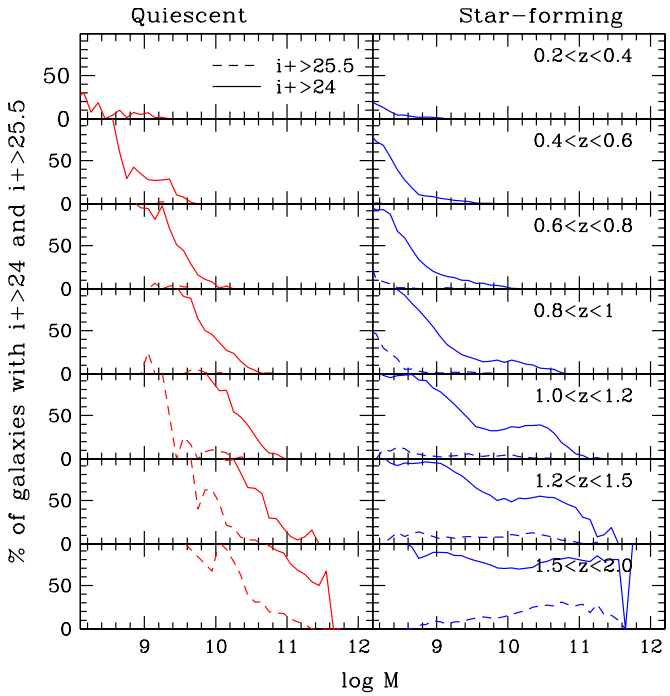

Figure 8. Fraction of galaxies with an apparent magnitude fainter than $i^+ = 24$ (solid lines) and $i^+ = 25.5$ (dashed lines) as a function of stellar mass. This fraction is measured per redshift bin (top to bottom panels). The left and right panels correspond to the quiescent and star-forming galaxies, respectively. From this fraction, we defined the lowest stellar mass limit which ensures a maximum of 30% of galaxies fainter than $i^+ > 24$ and $i^+ > 25.5$ in the lowest stellar mass bin of the MF.

(A color version of this figure is available in the online journal.)

defined the stellar mass ranges in order to keep the fraction of galaxies fainter than $i^+ > 25.5$ below an arbitrary limit of 30%. We set the limit to $i^+_{\rm AB} = 25.5$ since the photo-z are degraded at fainter magnitudes (Ilbert et al. 2009). With this approach, the lowest stellar mass bin of the MF has 30% of its objects with lower accuracy photo-z, and this fraction decreases rapidly in the higher stellar mass bins. According to Abraham et al. (2007) and Capak et al. (2007), the morphological classification is robust out to $i^+_{\rm AB} \sim 24$. When a morphological selection is applied, we therefore adopted a limit at $i^+_{\rm AB} < 24$ (solid line in Figure 8) rather than $i^+_{\rm AB} < 25.5$.

Moreover, Ilbert et al. (2004) and Fontana et al. (2004) showed that the MF estimators can be biased at low masses because galaxies with different SEDs (and mass-to-light ratios) are not visible up to the same stellar mass limit. This affects each MF estimator differently (see Figure 4 in Ilbert et al. 2004). We restricted our MF estimate to the stellar mass range where the three non-parametric estimators agree, to limit the impact of such bias on our results.

The lowest mass limits considered for the MF estimate are given in Tables 2 and 3 for each redshift bin. In all cases, the lowest limit in mass has to be the largest value imposed by the mix of galaxy type and the photo-z limitation at $i^+_{\rm AB} < 25.5$.

5. MF OF THE TOTAL SAMPLE

We first analyze the total MF (no cut by morphological or spectral type) and compare it with data from the literature. In the next sections, we will study the MF per morphological and spectral type (Figure 9 summarizes the different classifications used hereafter.)

Figure 10 shows the estimate of the total MF. The non-parametric MF estimate (open black circles) shows a small turn-over at $\log \mathcal{M} < 10$ and $z < 0.8$ which cannot be reproduced well with a Schechter function (Schechter 1976; see Appendix C). This turn-over is also detected in Pozzetti et al. (2009) and Drory et al. (2009). Therefore, we do not give a Schechter parameterization of the total MF. A parameterization can be retrieved by summing the Schechter fits of the "quiescent," "intermediate activity," and "high-activity" galaxies given in Tables 2 and 3. This sum (solid black curves in Figure 10) provides a parameterization in excellent agreement with the non-parametric estimate.

We compared the total MF and data from the literature (all MFs are converted into a Chabrier IMF and to the same cosmology). In general, we find excellent agreement between the different MFs out to $z = 2$. The offsets between the high-mass exponential cutoffs (i.e., the sharp decline of the density above the characteristic stellar mass $\mathcal{M}^*$) are smaller than 0.2 dex. Combined differences due to cosmic variance and methodology used to measure the stellar masses[17] are consistent with differences of 0.2 dex (see Section 4.2).

6. STELLAR MASS ASSEMBLY OF QUIESCENT AND ELLIPTICAL GALAXIES

In this section, we present the MF for galaxies having a "quiescent" spectral type. From the tight correlation seen in the local universe between morphology and colors, the quiescent galaxies are expected to preferentially have an elliptical morphology. However, the correlation between color and morphology is not perfect (Bell 2008), and we need to quantify how this relation evolves with redshift. Therefore, we also derived the MF of quiescent galaxies having an elliptical morphology ("red elliptical;" see Figure 9).

6.1. MF of Quiescent Galaxies

Figure 11 shows the MF of the quiescent galaxies in the range $z = 0.2$–2. We find that: (1) the density of "quiescent" galaxies more massive than $\log \mathcal{M} > 11$ increases by a factor of $\sim$14 between $z = 1.5$–2 and $z = 0.8$–1; (2) this evolution slows down significantly after $z < 1$ and the high-mass exponential cutoff does not increase by more than 0.2 dex at $z < 1$; (3) the density of quiescent galaxies increases at intermediate mass between $z = 0.8$–1 and $z = 0.2$–0.4 (e.g., by a factor of 4.4 at $\log \mathcal{M} \sim 10$). In Figure 12, we have over-plotted our results and the local measurement performed by Bell et al. (2003). We find consistent evolutionary trends when we compare our data to the local measurement[18]: the local density is higher at intermediate masses ($9 < \log \mathcal{M} < 11$) and the local exponential cutoff is consistent within 0.2 dex with the values obtained at $0.2 < z < 1$.

We analyze the evolution of the best-fit Schechter parameters of the quiescent MF (Table 2). The top panel of Figure 13 shows a continuous steepening of the slope α with time. This steepening reflects the rapid density increase of the low/intermediate mass galaxies. In the middle panel, the normalization Φ^* of the quiescent MF is shown to increase by a factor of 15 from

[17] For instance, Bundy et al. 2006 used the Charlot & Fall (2000) extinction law, Pozzetti et al. (2007) did not allow sub-solar metallicities, and Borch et al. (2006) used the PEGASE SPS package from Fioc & Rocca-Volmerange (1997) and no NIR data.

[18] The local MF is computed with the code PEGASE. The local MF could be shifted by +0.06 dex to match our stellar masses computed with the BC03 code (Rettura et al. 2006).

Table 2
Schechter Parameters of the MFs for the Quiescent and Elliptical Galaxies Between $z = 0.2$ and $z = 2$

Type	z-bin	Number	$\log \mathcal{M}_{\rm low}$	α	$\log \mathcal{M}^*$ ($\mathcal{M}_\odot$)	Φ^* (10^{-3} Mpc^{-3})	$\log \rho^*$ ($\mathcal{M}_\odot$ Mpc^{-3})
Quiescent	0.2–0.4	2202	8.8	$-0.91^{+0.02}_{-0.02}$	$11.13^{+0.03}_{-0.03}$	$1.12^{+0.07}_{-0.07}$	$8.16^{+0.04}_{-0.04}$
	0.4–0.6	1708	9.1	$-0.56^{+0.03}_{-0.03}$	$10.97^{+0.03}_{-0.03}$	$0.87^{+0.04}_{-0.04}$	$7.85^{+0.03}_{-0.03}$
	0.6–0.8	2432	9.4	$-0.25^{+0.04}_{-0.04}$	$10.83^{+0.02}_{-0.02}$	$1.15^{+0.03}_{-0.03}$	$7.86^{+0.02}_{-0.02}$
	0.8–1.0	3381	9.3	$0.04^{+0.03}_{-0.03}$	$10.77^{+0.01}_{-0.01}$	$1.43^{+0.03}_{-0.03}$	$7.94^{+0.02}_{-0.02}$
	1.0–1.2	1447	9.6	$0.25^{+0.08}_{-0.08}$	$10.70^{+0.03}_{-0.02}$	$0.55^{+0.02}_{-0.02}$	$7.49^{+0.02}_{-0.02}$
	1.2–1.5	1069	10.1	0.50	$10.64^{+0.14}_{-0.13}$	$0.26^{+0.02}_{-0.02}$	$7.17^{+0.02}_{-0.02}$
	1.5–2.0	468	10.7	0.50	$10.67^{+0.10}_{-0.10}$	$0.10^{+0.02}_{-0.04}$	$6.78^{+0.03}_{-0.03}$
Red sequence	0.2–0.4	2343	8.8	$-1.03^{+0.04}_{-0.04}$	$11.18^{+0.05}_{-0.05}$	$0.86^{+0.14}_{-0.14}$	$8.12^{+0.05}_{-0.05}$
	0.4–0.6	2000	9.1	$-0.66^{+0.03}_{-0.03}$	$10.97^{+0.03}_{-0.03}$	$0.88^{+0.05}_{-0.05}$	$7.86^{+0.03}_{-0.03}$
	0.6–0.8	2752	9.4	$-0.46^{+0.03}_{-0.03}$	$10.86^{+0.02}_{-0.02}$	$1.09^{+0.04}_{-0.04}$	$7.84^{+0.02}_{-0.02}$
	0.8–1.0	4108	9.3	$-0.07^{+0.03}_{-0.03}$	$10.73^{+0.01}_{-0.01}$	$1.66^{+0.04}_{-0.04}$	$7.94^{+0.02}_{-0.02}$
	1.0–1.2	2624	9.6	$0.18^{+0.06}_{-0.06}$	$10.65^{+0.02}_{-0.02}$	$1.00^{+0.03}_{-0.03}$	$7.69^{+0.02}_{-0.02}$
	1.2–1.5	2568	10.1	0.50	$10.56^{+0.013}_{-0.11}$	$0.64^{+0.03}_{-0.12}$	$7.49^{+0.02}_{-0.02}$
	1.5–2.0	1545	10.7	0.50	$10.63^{+0.09}_{-0.09}$	$0.35^{+0.05}_{-0.08}$	$7.30^{+0.03}_{-0.03}$
Red elliptical	0.2–0.4	1396	8.8	$-0.76^{+0.03}_{-0.03}$	$11.02^{+0.03}_{-0.03}$	$1.37^{+0.09}_{-0.09}$	$8.12^{+0.04}_{-0.04}$
	0.4–0.6	1020	9.1	$-0.35^{+0.04}_{-0.04}$	$10.86^{+0.03}_{-0.03}$	$0.90^{+0.04}_{-0.04}$	$7.77^{+0.03}_{-0.03}$
	0.6–0.8	1538	9.7	$-0.04^{+0.06}_{-0.06}$	$10.75^{+0.02}_{-0.02}$	$1.18^{+0.03}_{-0.03}$	$7.81^{+0.02}_{-0.02}$
	0.8–1.0	1902	10.1	$0.04^{+0.08}_{-0.08}$	$10.75^{+0.03}_{-0.02}$	$1.28^{+0.03}_{-0.03}$	$7.86^{+0.02}_{-0.02}$
	1.0–1.2	480	10.6	0.50	$10.65^{+0.09}_{-0.09}$	$0.39^{+0.05}_{-0.05}$	$7.36^{+0.04}_{-0.05}$
Blue elliptical	0.2–0.4	1484	8.8	$-1.29^{+0.03}_{-0.03}$	$11.10^{+0.09}_{-0.08}$	$0.32^{+0.05}_{-0.05}$	$7.71^{+0.06}_{-0.09}$
	0.4–0.6	1474	9.1	$-1.24^{+0.03}_{-0.03}$	$11.09^{+0.07}_{-0.06}$	$0.22^{+0.03}_{-0.03}$	$7.52^{+0.05}_{-0.06}$
	0.6–0.8	1306	9.7	$-1.10^{+0.06}_{-0.06}$	$10.93^{+0.05}_{-0.05}$	$0.35^{+0.05}_{-0.05}$	$7.49^{+0.03}_{-0.03}$
	0.8–1.0	1160	10.1	$-0.23^{+0.13}_{-0.12}$	$10.58^{+0.04}_{-0.04}$	$0.87^{+0.04}_{-0.04}$	$7.48^{+0.02}_{-0.02}$
	1.0–1.2	468	10.6	-1.00	$10.87^{+0.13}_{-0.14}$	$0.39^{+0.07}_{-0.07}$	$7.47^{+0.18}_{-0.19}$
Elliptical	0.2–0.4	2880	8.8	$-1.06^{+0.02}_{-0.02}$	$11.13^{+0.04}_{-0.03}$	$1.28^{+0.09}_{-0.09}$	$8.26^{+0.04}_{-0.04}$
	0.4–0.6	2494	9.1	$-0.95^{+0.02}_{-0.02}$	$11.06^{+0.03}_{-0.03}$	$0.81^{+0.05}_{-0.05}$	$7.96^{+0.03}_{-0.03}$
	0.6–0.8	2844	9.7	$-0.61^{+0.04}_{-0.04}$	$10.87^{+0.02}_{-0.02}$	$1.44^{+0.07}_{-0.07}$	$7.98^{+0.02}_{-0.02}$
	0.8–1.0	3062	10.1	$-0.20^{+0.06}_{-0.06}$	$10.74^{+0.02}_{-0.02}$	$2.00^{+0.05}_{-0.06}$	$8.01^{+0.01}_{-0.01}$
	1.0–1.2	948	10.6	-0.30	$10.76^{+0.13}_{-0.10}$	$0.93^{+0.06}_{-0.12}$	$7.68^{+0.09}_{-0.05}$

Notes. The errors combined the 1σ Poissonian errors ($2\Delta\ln\mathcal{L} = 1$) as well as the uncertainties induced by the photo-z. Parameters α listed without errors are set "ad hoc," and the errors on $\log \mathcal{M}^*$ and Φ^* are obtained by varying α by ± 0.5 around the fixed value. The morphological classification is obtained using the G–C parameters. However, we caution the reader that the errors are probably underestimated: the error budget is dominated by systematic effects (e.g., possible photo-z biases, systematic uncertainties related to the stellar mass estimate) that are not included here.

$z = 1.5$–2 to $z = 0.8$–1. The rapid increase of Φ^* is no longer detected from $z = 0.8$–1 to $z = 0.2$–0.4 where Φ^* remains approximately constant. Some fluctuations (a factor of $\sim$2) appear in this redshift range when we reduce the size of the redshift bins to $\Delta z = 0.1$, which is consistent with cosmic variance (Scoville et al. 2007). Finally, the characteristic stellar mass $\mathcal{M}^*$ increases by 0.3–0.4 dex between $z \sim 1$ and $z \sim 0.3$ (bottom panel).

6.2. MF of Red Elliptical Galaxies

Figure 11 shows the MF of the red ellipticals (quiescent with an elliptical morphology) galaxies in the range $z = 0.2$–1.2. We find a similar evolution for the red ellipticals as for the quiescent galaxies. Between $z = 0.8$–1 and $z = 0.2$–0.4, the density of red ellipticals increases by a factor of 4–5.4 at intermediate mass ($\log \mathcal{M} \sim 10$). By contrast, their density increases only by 1.7–2 at high mass ($\log \mathcal{M} > 11$). Therefore, the most massive red elliptical galaxies show little evolution at $z < 1$ while their density still increases at low/intermediate masses.

The ratio between the red elliptical and quiescent MFs is plotted in Figure 14. This ratio quantifies the fraction of quiescent galaxies with an elliptical morphology (and the complementary information about the fraction of Spi/Irr with quenched star formation). At high mass, $\log \mathcal{M} \sim 11$, the fraction of quiescent galaxies with an elliptical morphology is greater than 90% (80%) at $z < 0.8$ for a G–C (C09) classification. This fraction has a maximum at $10.5 < \log \mathcal{M} < 11$ and decreases continuously toward low masses reaching 60% (40%) at $\log \mathcal{M} \sim 9.5$. This fraction seems also to decrease at really high mass ($\log \mathcal{M} \sim 11.5$). However, we caution the reader that the constraint on the MF at such high masses relies on few galaxies.

The fraction of quiescent galaxies with an elliptical morphology decreases at $z > 0.8$ (Figure 14). This decrease is seen with both classifications. The decrease is much faster if we consider the C09 classification which is more conservative in selecting pure elliptical galaxies. This trend could show that: the fraction of Spi/Irr with a quenched SFR increases with redshift ; the "red and dead" local elliptical galaxies did not have fully acquired their elliptical morphology at $z > 0.8$. This result is discussed in Bundy et al. (2009) and Oesch et al. (2009).

Table 3
Schechter Parameters of Star-forming Galaxies ("Intermediate Activity," "High Activity") Between $z = 0.2$ and $z = 2$

Type	z-bin	Number	$\log \mathcal{M}_{\rm low}$	α	$\log \mathcal{M}^*$ ($\mathcal{M}_\odot$)	Φ^* (10^{-3} Mpc^{-3})	$\log \rho^*$ ($\mathcal{M}_\odot$ Mpc^{-3})
Intermediate	0.2–0.4	5410	8.8	$-1.20^{+0.02}_{-0.02}$	$10.96^{+0.03}_{-0.03}$	$1.31^{+0.09}_{-0.09}$	$8.14^{+0.03}_{-0.03}$
activity	0.4–0.6	4346	9.1	$-1.02^{+0.02}_{-0.02}$	$10.93^{+0.03}_{-0.03}$	$0.96^{+0.06}_{-0.06}$	$7.92^{+0.02}_{-0.03}$
	0.6–0.8	4837	9.3	$-0.90^{+0.03}_{-0.03}$	$10.85^{+0.02}_{-0.02}$	$1.02^{+0.06}_{-0.06}$	$7.84^{+0.02}_{-0.02}$
	0.8–1.0	5242	9.4	$-0.54^{+0.03}_{-0.03}$	$10.73^{+0.02}_{-0.02}$	$1.52^{+0.07}_{-0.07}$	$7.86^{+0.02}_{-0.02}$
	1.0–1.2	3826	9.5	$-0.44^{+0.04}_{-0.04}$	$10.77^{+0.02}_{-0.02}$	$1.05^{+0.04}_{-0.04}$	$7.74^{+0.02}_{-0.02}$
	1.2–1.5	4741	9.6	$-0.88^{+0.04}_{-0.04}$	$10.94^{+0.03}_{-0.03}$	$0.45^{+0.03}_{-0.03}$	$7.57^{+0.02}_{-0.02}$
	1.5–2.0	5019	9.8	$-1.03^{+0.04}_{-0.04}$	$11.02^{+0.03}_{-0.03}$	$0.23^{+0.02}_{-0.02}$	$7.40^{+0.02}_{-0.02}$
High	0.2–0.4	2231	8.7	$-1.51^{+0.04}_{-0.04}$	$10.42^{+0.07}_{-0.07}$	$0.36^{+0.06}_{-0.06}$	$7.23^{+0.03}_{-0.04}$
activity	0.4–0.6	4626	8.8	$-1.47^{+0.03}_{-0.03}$	$10.39^{+0.05}_{-0.05}$	$0.46^{+0.06}_{-0.06}$	$7.28^{+0.02}_{-0.02}$
	0.6–0.8	10,261	8.9	$-1.48^{+0.02}_{-0.02}$	$10.49^{+0.03}_{-0.03}$	$0.65^{+0.05}_{-0.05}$	$7.53^{+0.01}_{-0.02}$
	0.8–1.0	12,686	9.0	$-1.33^{+0.02}_{-0.02}$	$10.48^{+0.02}_{-0.02}$	$1.00^{+0.06}_{-0.06}$	$7.61^{+0.01}_{-0.01}$
	1.0–1.2	10,335	9.2	$-1.29^{+0.02}_{-0.02}$	$10.48^{+0.02}_{-0.02}$	$0.93^{+0.06}_{-0.06}$	$7.56^{+0.01}_{-0.01}$
	1.2–1.5	14,609	9.2	$-1.26^{+0.02}_{-0.02}$	$10.54^{+0.02}_{-0.02}$	$0.79^{+0.04}_{-0.04}$	$7.53^{+0.01}_{-0.01}$
	1.5–2.0	8697	9.8	-1.30	$10.75^{+0.70}_{-0.3}$	$0.39^{+0.3}_{-0.3}$	$7.45^{+0.23}_{-0.16}$

Notes. A parameterization of the total MF can be retrieved by summing the Schechter fit of the "quiescent" (given in Table 2), "intermediate activity," and "high activity" galaxies. Errors are computed as in Table 2.

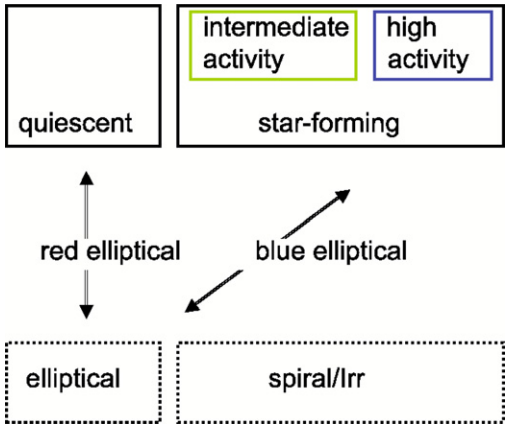

Figure 9. Schematic view of the different classifications used in this paper. The top and bottom panels are the spectral and morphological classifications, respectively.

(A color version of this figure is available in the online journal.)

6.3. Stellar Mass Density of Quiescent and Red Elliptical Galaxies

The stellar mass density quantifies the total stellar mass locked up in a given population ($\rho = \int_{10^5}^{10^{13}} \phi(\mathcal{M}) d\mathcal{M}$).

The stellar mass density of quiescent galaxies (shown in Figure 15) increases by 1.1 dex (a factor of 14) between $z = 1.5$–2 and $z = 0.8$–1, and still increases by 0.2 dex between $z = 0.8$–1 and $z = 0.2$–0.4 (by 0.3 dex if we consider the local measurement by Bell et al. 2003). Therefore, the stellar mass assembly of quiescent galaxies appears to slow down at $z < 1$.

Figure 15 shows the stellar mass density of red elliptical galaxies. The lower and upper limits of the shaded areas correspond to the C09 and G–C morphological classifications, respectively. At $z < 0.8$, the total stellar mass of red elliptical galaxies contributes more than 80% (70%) of the total stellar mass in quiescent galaxies.

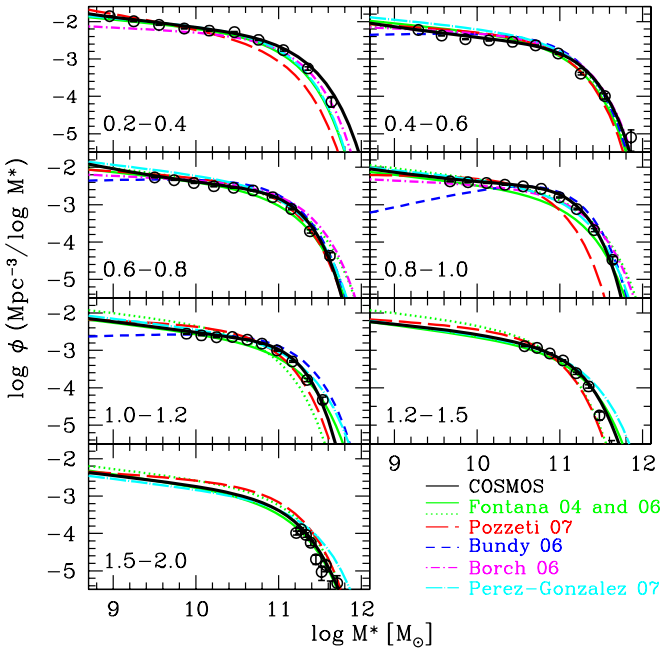

Figure 10. Total MF (no separation by type). The open circles are the non-parametric estimates of the MF ($1/V_{\rm max}$). The solid black lines are the sum of the "quiescent," "intermediate activity," and "high activity" MFs as taken from Tables 2 and 3. The total MFs are compared with data from the literature (all MFs are converted into a Chabrier IMF).

(A color version of this figure is available in the online journal.)

6.4. Comparison with the Literature

Figure 16 compares our "quiescent" MFs with those from the literature. The K-band luminosity functions from Cirasuolo et al. (2007) and Arnouts et al. (2007) are converted into stellar MFs using the mass-to-light ratio given in Arnouts et al. (2007).

Most of the MFs from the literature are derived for red sequence galaxies. Therefore, we split the COSMOS sample into "red sequence" and "blue cloud" galaxies according to the empirical limit $M_{\rm NUV} - M_R = 0.5 \log \mathcal{M} - 0.8\ z - 0.5$ (see

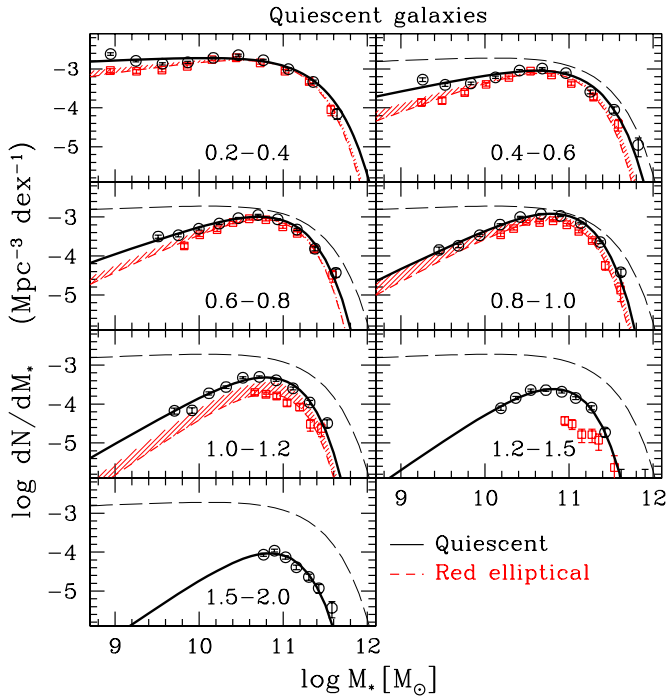

Figure 11. Evolution of the MFs for "quiescent" galaxies from $z = 0.2$–0.4 (top left panel) to $z = 1.5$–2 (bottom left panel). The "quiescent" galaxies are shown by black open circles and solid lines. The lower and upper envelopes of the shaded area are the red elliptical classified using C09 and G–C, respectively. The black long-dashed line is the quiescent MF estimated at $z = 0.2$–0.4; it is shown in each panel to serve as a reference.

(A color version of this figure is available in the online journal.)

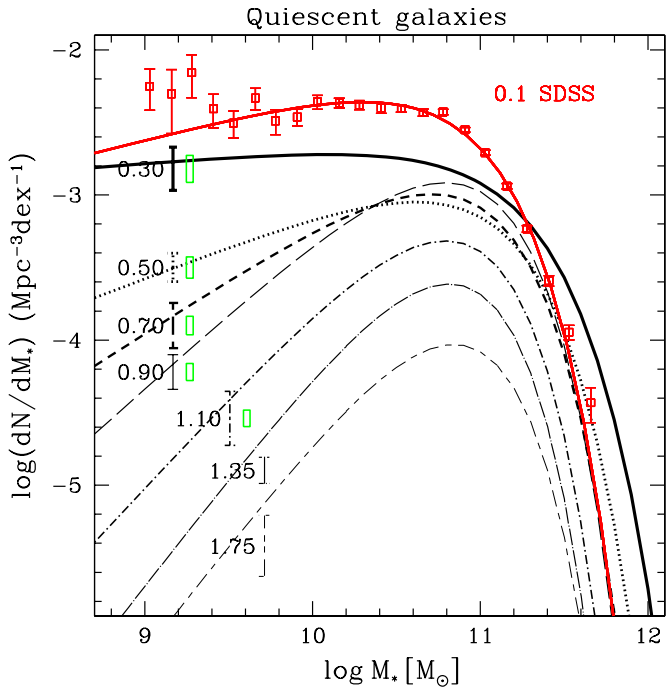

Figure 12. MF of the "quiescent" galaxies from $z = 1.5$–2 to $z = 0.2$–0.4. The numbers on the MFs are the redshifts. The green vertical boxes are an estimate of the cosmic variance by Scoville et al. (2007) for halo mass ranges of 10^{13}–10^{14} $\mathcal{M}_{\odot}$. The black vertical lines correspond to the two extreme MFs in four sub-fields obtained by splitting the 2 deg^2 into four quadrants each of 0.5 deg^2. The red solid line and points are the local MF measurements for red galaxies by Bell et al. (2003) at $z \sim 0.1$.

(A color version of this figure is available in the online journal.)

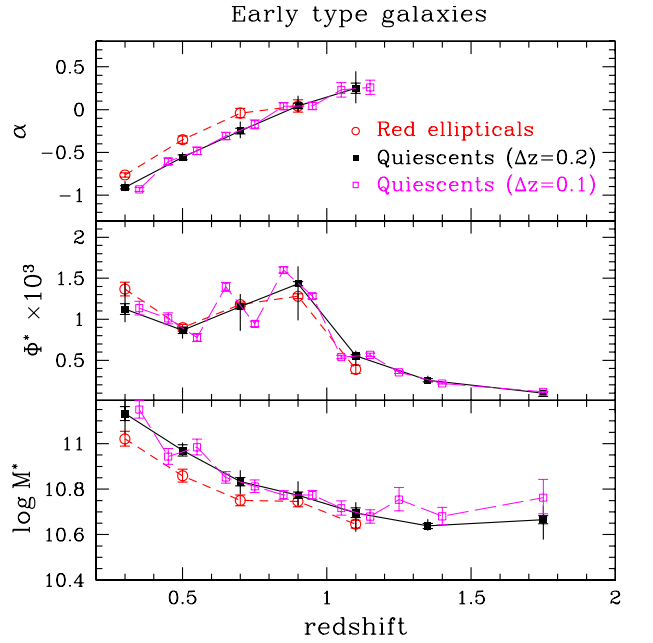

Figure 13. Evolution of the Schechter parameters as a function of redshift (black solid lines: quiescent; red dashed lines: red ellipticals). The long-dashed magenta lines show the Schechter parameters measured in smaller redshift bins of $\Delta z = 0.1$ for the quiescent galaxies. From the top to the bottom panel: evolution with redshift of the slope, the normalization, and the characteristic stellar mass, respectively. The vertical lines for the quiescent galaxies represent the extreme values in four sub-fields of 0.5 deg^2 after having divided the COSMOS field into four equal quadrants.

(A color version of this figure is available in the online journal.)

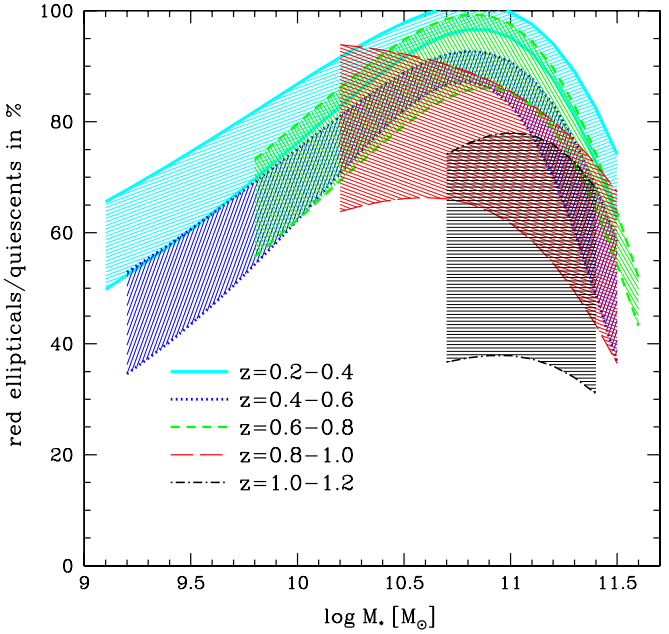

Figure 14. Fraction (in %) of "quiescent" galaxies with an elliptical morphology. The fraction is obtained by dividing the MF of the red ellipticals by the MF of the quiescent galaxies. The upper and lower limits are obtained using the G–C and C09 morphological classifications, respectively.

(A color version of this figure is available in the online journal.)

Figure 20). Our MFs for red sequence galaxies (open triangles in Figure 16) are systematically higher at $z > 1$ than our MFs for quiescent galaxies (open circles). We interpret this difference as being due to the presence of dust-extincted spirals within the red sequence (see also Figure 5). This contamination of the red sequence could increase with redshift since the density of dusty

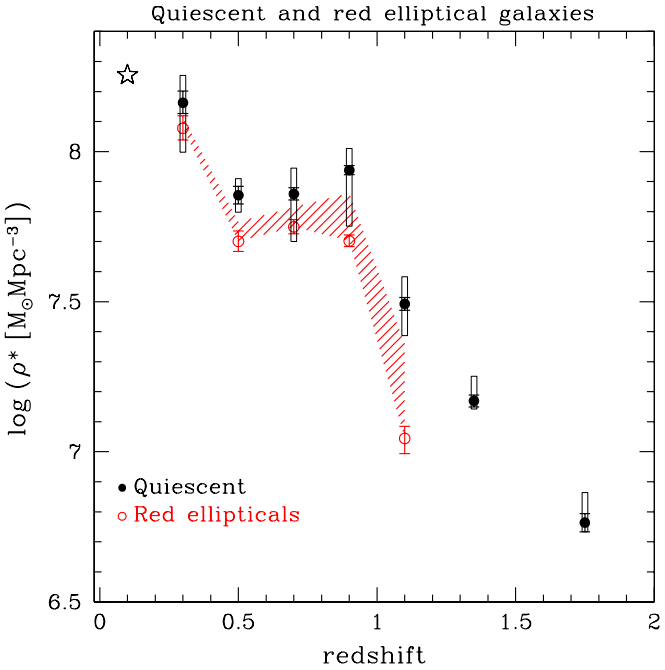

Figure 15. Stellar mass density of quiescent galaxies (black solid circles) and red ellipticals (red open circles). The lower and upper envelopes of the shaded area correspond to the stellar mass density computed using the C09 and G–C classifications, respectively. The open star is the local measurement by Bell et al. (2003). The vertical boxes for the quiescent correspond to the two extreme values measured in four quadrants of 0.5 deg^2.

(A color version of this figure is available in the online journal.)

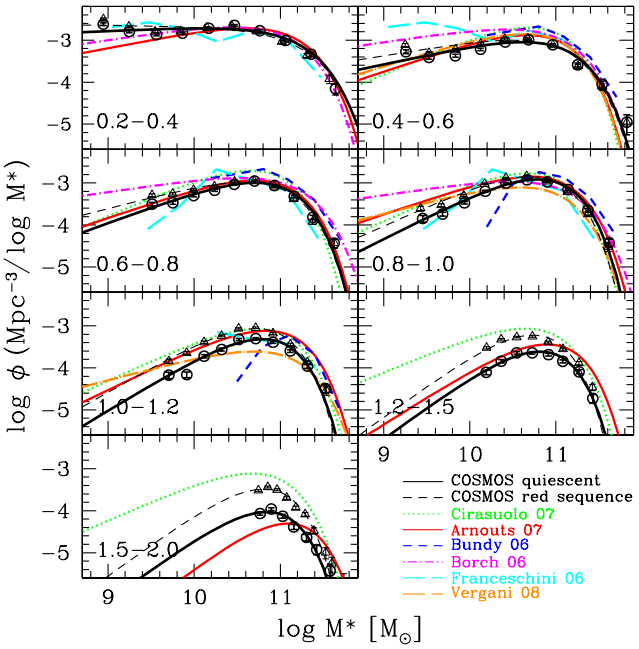

Figure 16. Comparison between our MFs derived for quiescent (black open circles) and red sequence (open triangles) galaxies and the MFs from the literature. The MFs measured by Arnouts et al. (2007; solid red curves) are based on a template-fitting classification. The MFs measured by Cirasuolo et al. (2007; green dotted lines) are obtained using a red sequence classification.

(A color version of this figure is available in the online journal.)

star-forming galaxies increases with redshift (e.g., Takeuchi et al. 2005; Le Floc'h et al. 2005).

The agreement between the various surveys at the high-mass end is good (within 0.2 dex), given the uncertainties in the stellar masses, the different classification methods, and

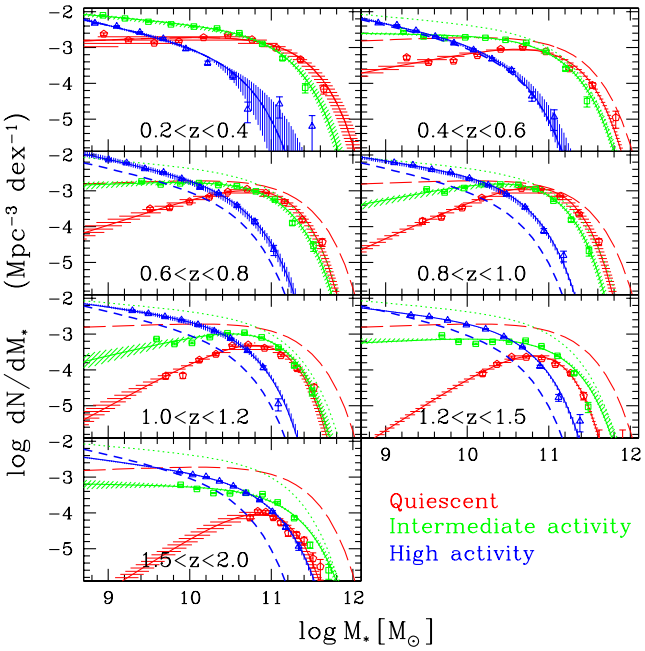

Figure 17. MF by spectral type. The sample is split into "high activity" (blue vertical shaded area), "intermediate activity" (green oblique shaded area), and "quiescent" (red horizontal shaded area) galaxies. The lower and upper limits of the shaded areas are the extreme values of the MFs estimated in four quadrants of 0.5 deg^2, which quantifies the impact of cosmic variance. The blue short-dashed lines, the green dotted lines, and the red long-dashed lines are the MFs measured at $z = 0.2$–0.4 for the "high activity," "intermediate activity," and "quiescent" galaxies, respectively.

(A color version of this figure is available in the online journal.)

cosmic variance. The increase of massive red galaxies between $z = 1.5$–2 and $z = 0.8$–1 has also been seen in previous studies (e.g., Cirasuolo et al. 2007; Arnouts et al. 2007). However, the amplitude of this increase differs between the samples. At $z = 1.5$–2, the MF normalization derived by Cirasuolo et al. (2007) is a factor ~10 higher than Arnouts et al. (2007). Our MFs for red sequence (open triangles) and quiescent galaxies (open circles) show that the two measurements can be partly reconciled when consistent selection criteria are applied (Cirasuolo et al. used red sequence galaxies and Arnouts et al. used a template-fitting classification close to our quiescent definition).

7. STELLAR MASS ASSEMBLY OF STAR-FORMING GALAXIES

This section presents the MF and stellar mass density for star-forming galaxies. We subdivided the star-forming sample into "intermediate activity" and "high activity" galaxies using a best-fit template procedure (see Section 3.2 and Figure 9). We did not attempt to introduce a morphological separation since it would require a too fine classification within the Spi/Irr population.

7.1. MF of Star-forming Galaxies

Figure 17 shows the MF evolution of the "intermediate activity" (green oblique shaded area) and "high activity" galaxies (blue vertical shaded area). The MF of the "quiescent" galaxies (red horizontal shaded area; see Section 6) is added as a reference. Both the MFs of "intermediate activity" and "high activity" galaxies evolve between $z = 2$ and $z = 0.2$. Since their shapes change with time, this evolution is mass-dependent.

As a consistent trend at all redshifts, the slope of the "high activity" galaxies is always the steepest. The density of "high

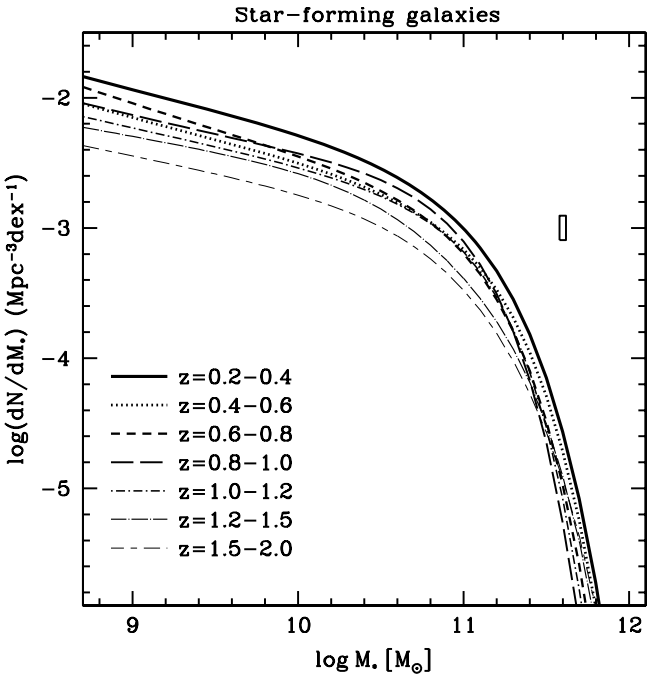

Figure 18. MF of "star-forming" galaxies (sum of intermediate and high activity galaxies) from $z = 2$ to $z = 0.2$. The vertical box quantifies the cosmic variance at $z = 0.2$–0.4 (Scoville et al. 2007).

activity" galaxies decreases with cosmic time but the size of this decrease is a strong function of the stellar mass. Between $z = 1.2$–1.5 and $z = 0.2$–0.4, their number density decreases by a factor of 5 at $\log \mathcal{M} > 11$, and only by a factor of 1.1 at $9.5 < \log \mathcal{M} < 10$.

The "intermediate activity" MF follows a different evolution. Galaxies as massive as $\log \mathcal{M} \sim 11.6$ are already in place at $z = 1.5$–2. The density of lower mass galaxies rises with times.

We plotted in Figure 18 the MFs of all star-forming galaxies, i.e., the sum of the "intermediate activity" and "high activity" MFs. The exponential cutoff does not evolve by more than 0.2 dex between $z = 1.2$–1.5 and $z = 0.2$–0.4, which is consistent with cosmic variance and systematic errors in stellar mass measurements. We do not observe significant changes in the MF shape. Therefore, the decrease with time of "high activity" galaxies is partly counter-balanced by the buildup of the "intermediate activity" MF.

7.2. Stellar Mass Density of Star-forming Galaxies

Figure 19 shows the evolution of the integrated stellar mass density for "intermediate activity" (green triangles), "high activity" (blue squares), and all star-forming galaxies (sum of intermediate and high activity: open circles).

The stellar mass density increases between $z = 1.5$–2 and $z = 0.8$–1 for star-forming populations. The density increases by 0.5 dex, 0.2 dex, and 0.3 dex for the "intermediate activity," the "high activity," and all star-forming galaxies, respectively.

The "intermediate activity" and "high activity" galaxies follow an opposite evolution at $z < 1$. Between $z = 0.8$–1 and $z = 0.2$–0.4, the stellar mass density increases by 0.3 dex for the "intermediate activity" galaxies, while it decreases by 0.4 dex for the "high activity" galaxies. The stellar mass density of all star-forming galaxies shows little evolution at $z < 1$. Indeed, the stellar mass density at $z \sim 0.1$ measured by Bell et al. (2003) for star-forming galaxies is consistent with the stellar mass density we measure at $z \sim 1$.

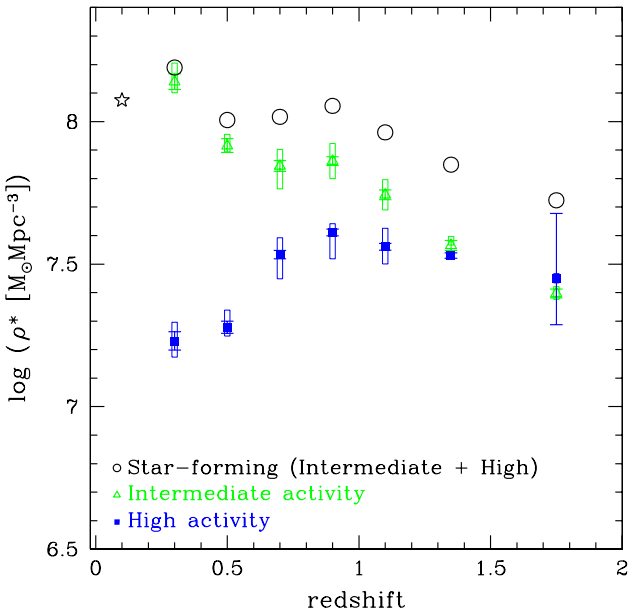

Figure 19. Stellar mass density of star-forming galaxies. The green open triangles and the blue solid squares are the "intermediate activity" and "high activity" galaxies, respectively. The black open circles are all star-forming galaxies (sum of "high activity" and "intermediate activity"). The open star is the local measurement by Bell et al. (2003). The boxes correspond to the two extreme values measured in four quadrants of 0.5 deg^2.

(A color version of this figure is available in the online journal.)

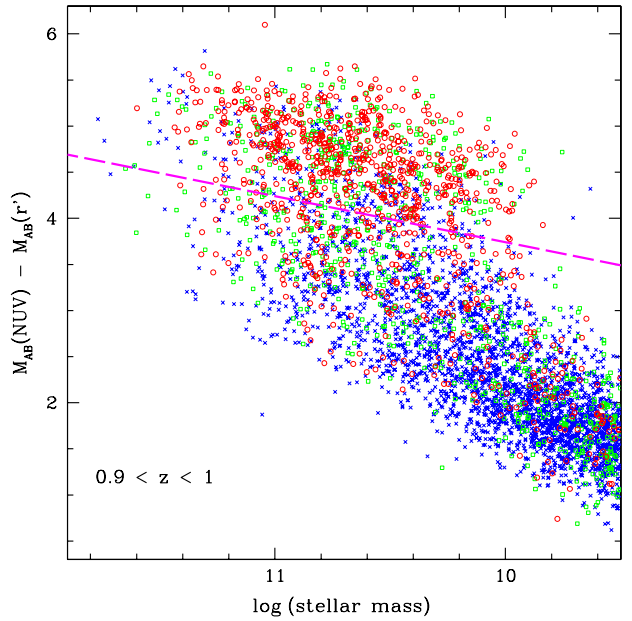

Figure 20. Rest-frame color $M(\mathrm{NUV}) - M(r^+)$ (not corrected for dust reddening) as a function of stellar mass at $i^+ < 24$ in a given redshift bin $0.9 < z < 1$. The red open circles are the galaxies morphologically selected as elliptical by C09. The green open squares are selected as elliptical with the G–C parameters and not by C09. The blue crosses are Spi/Irr galaxies classified with the G–C parameters. The magenta dashed line is the limit adopted to split the sample into red sequence and blue cloud galaxies.

(A color version of this figure is available in the online journal.)

8. STAR-FORMING GALAXIES WITH AN ELLIPTICAL MORPHOLOGY

As shown in Figure 20, the elliptical galaxies preferentially have a red color. However, a significant population of elliptical galaxies appears to be blue. The presence of "blue elliptical" is not unexpected. The "blue elliptical" galaxies could be newly

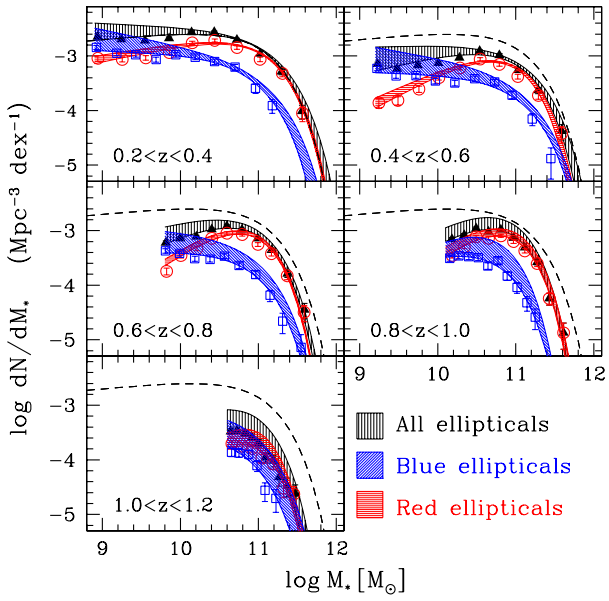

Figure 21. MF of elliptical galaxies selected in morphology without any cut in color (black vertical shaded area). The blue oblique shaded areas and the horizontal red shaded areas are the MFs of the blue and red elliptical galaxies, respectively. The upper and lower envelope MFs are obtained using the G–C and C09 morphological classifications, respectively. For clarity in the figure, the non-parametric estimates are shown only for the C09 classification. The dashed line is the MF of elliptical galaxies derived at $z = 0.2$–0.4, which is shown in each redshift bin to serve as a reference.

(A color version of this figure is available in the online journal.)

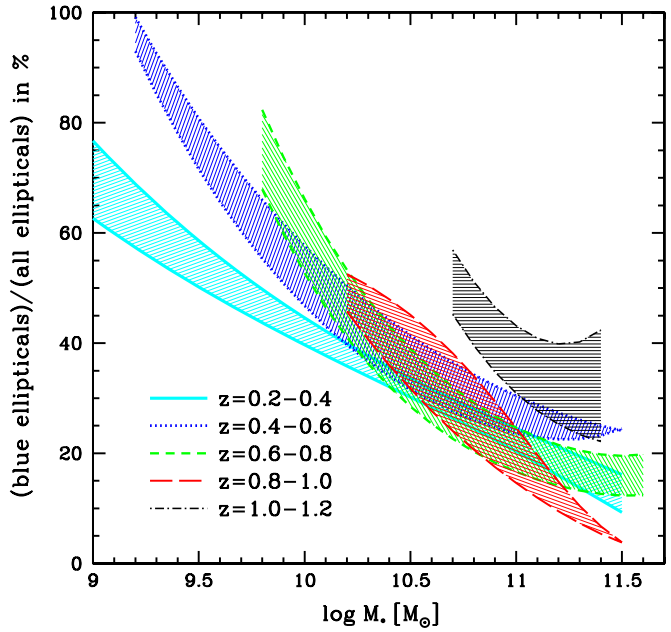

Figure 22. Fraction (in %) of blue galaxies in the elliptical sample (morphologically selected). The upper and lower limits are obtained using the G–C and C09 morphological classifications, respectively.

(A color version of this figure is available in the online journal.)

formed elliptical galaxies still consuming the gas of their progenitors. Accretion of new cold gas into an old elliptical galaxy (Hammer et al. 2007) could also produce a blue color. We present here the MF of this elliptical population which is star forming.

Figure 21 shows the MFs of the elliptical galaxies purely selected by morphology (black vertical shaded area), the "blue elliptical" galaxies (blue shaded area), and the red elliptical galaxies (red shaded area). The shape of the "blue elliptical" MFs differs from those of the red elliptical galaxies: the slope is steeper and the exponential cutoff is shifted to lower mass (in agreement with Ilbert et al. 2006a). As a consequence of these different shapes, the contribution of the "blue elliptical" galaxies to the total elliptical population depends strongly on stellar mass. Figure 22 shows that, regardless of redshift, the fraction of "blue ellipticals" decreases toward high mass systems. The "blue elliptical" galaxies represent <20% of the massive elliptical galaxies (at $\log \mathcal{M} > 11$ and $z < 1$), but their contribution reaches 40%–60% at $\log \mathcal{M} \sim 10$.

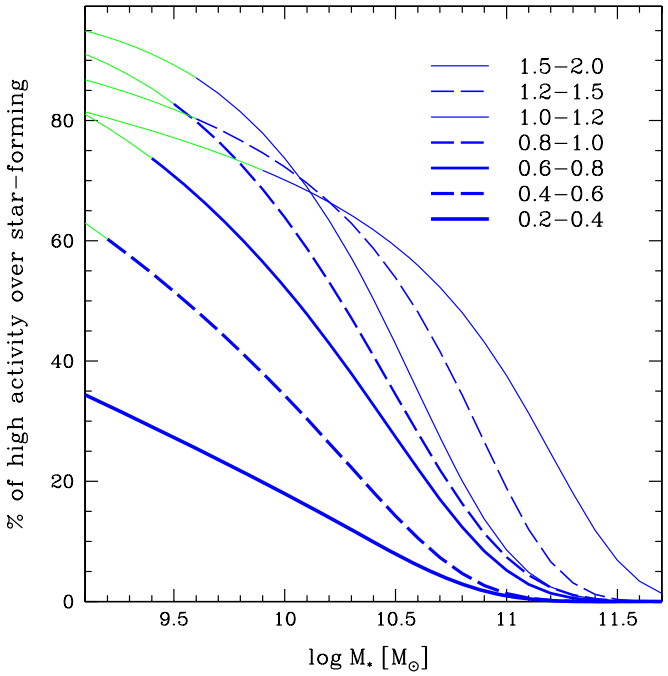

Figure 23. Fraction in % of "high activity" galaxies within the star-forming sample as a function of the stellar mass and per redshift bin (MF of the "high activity" divided by the MF of all star-forming galaxies). The thick blue line corresponds to the stellar mass range covered by the data. The thin green line is obtained using the extrapolation of the MF with a Schechter function.

(A color version of this figure is available in the online journal.)

9. DISCUSSION

9.1. Redistribution of the Star Formation Activity Along Cosmic Time

We first discuss our results on the MF of star-forming galaxies.

The total stellar mass of "high activity" galaxies decreases by a factor of 1.7 between $z = 1.5$–2 and $z = 0.2$–0.4 (see Section 7), while the stellar mass of a given star-forming galaxy grows. A simple interpretation is that, after an intense star formation activity period, these galaxies evolve into less active systems (intermediate activity or quiescent). Based on the BC03 models, a passive evolution could transform a "high activity" galaxy at $z \sim 1.5$ into an "intermediate activity" galaxy at $z \sim 0.7$.[19]

Figure 23 shows the fraction of "high activity" galaxies within the star-forming sample. This fraction does not decrease uniformly at all stellar masses. Between $z = 1.5$–2 and $z = 1$–1.2, the fraction of "high activity" galaxies at $\log \mathcal{M} \sim 11$ drops by a factor of ~4 (from 40% to 10%), while the fraction

[19] A galaxy with a rest-frame color $(\mathrm{NUV} - r^+)_{\mathrm{template}} \sim 1$ reddens by 2 mag in 3 Gyr assuming an exponentially decreasing SFR with $\tau = 1$ Gyr and a solar metallicity.

stays approximately constant at low mass $\log \mathcal{M} \sim 9.5$–10. The contribution of low mass, high activity galaxies starts to decrease significantly only at $z < 1$. Since each spectral type corresponds to a range of SSFR (see Section 3.2), it implies that the low mass star-forming galaxies are able to maintain a high SSFR, while the massive galaxies evolve rapidly into systems with a lower SSFR. Therefore, the redistribution of the star formation activity follows a clear "downsizing" pattern (Cowie et al. 1996) within the star-forming sample itself.

The MF of all star-forming galaxies (sum of intermediate and high activity) shows little evolution between $z \sim 1.5$ and $z \sim 0.2$. The redistribution of the star formation activity between "intermediate activity" and "high activity" galaxies does not affect the overall mass distribution of the star-forming galaxies. The little evolution of the star-forming MF means that a fraction of star-forming galaxies is transferred to the quiescent population (as already noted by Arnouts et al. 2007 and Cowie & Barger 2008), since star-forming galaxies generate new stellar populations between $z \sim 1.5$ and $z \sim 0.2$. Using backward evolution models, Boissier et al. (2009) discuss in detail the consistency between the little evolution of the star-forming MF and the building of the quiescent population. We discuss in the next sections which processes can generate these quiescent systems.

9.2. Mass-dependent Assembly of Elliptical Galaxies at $z < 1$

We find that the most massive quiescent galaxies are already in place at $z \sim 1$ while their density still rises at low/intermediate masses at $z < 1$ (see Section 6). This mass-dependent evolution of quiescent galaxies confirms the "downsizing" pattern found by the COMBO-17 survey (Borch et al. 2006) and the DEEP2 survey (Bundy et al. 2006; Cimatti et al. 2006). We also investigated the MF evolution of the quiescent galaxies with an elliptical morphology. We retrieved the same downsizing pattern: the most massive red elliptical galaxies are already in place at $z \sim 1$, while the low/intermediate mass red E/S0 galaxies are still being created at $z < 1$. In principle, the weak evolution of the massive red elliptical galaxies at $z < 1$ could be explained by a selection procedure based on the galaxy spectra (Van Dokkum & Franx 2001) since blue elliptical galaxies missed by a multi-color criterion could account for a significant evolution of the high-mass end. However, we showed in Section 6 that the contribution of blue elliptical galaxies is limited to 20% at $\log \mathcal{M} > 11$. Therefore, the blue elliptical contribution cannot explain the low evolution rate of the most massive elliptical galaxies at $z < 1$.

A possible interpretation of this mass dependent evolution is a galaxy assembly by merger process more efficient at low/intermediate mass than at high mass at $z < 1$, if we assume that red elliptical galaxies are formed by mergers (e.g., Toomre & Toomre 1972; Athanassoula 2008; Bekki 2008).[20] This picture is in agreement with De Ravel et al. (2009) who found that the merger rate decreases with stellar mass when using galaxy pair counts in the VIMOS-VLT Deep Survey (Le Fèvre et al. 2005).

The formation of low mass quiescent galaxies with an elliptical morphology could also be explained by "morphological quenching" (Martig et al. 2009). The presence of a spheroid is sufficient to stabilize the gas disk and quench the star formation. This process is efficient in low mass halos which could explain the formation of these low mass, quiescent, and elliptical galaxies.

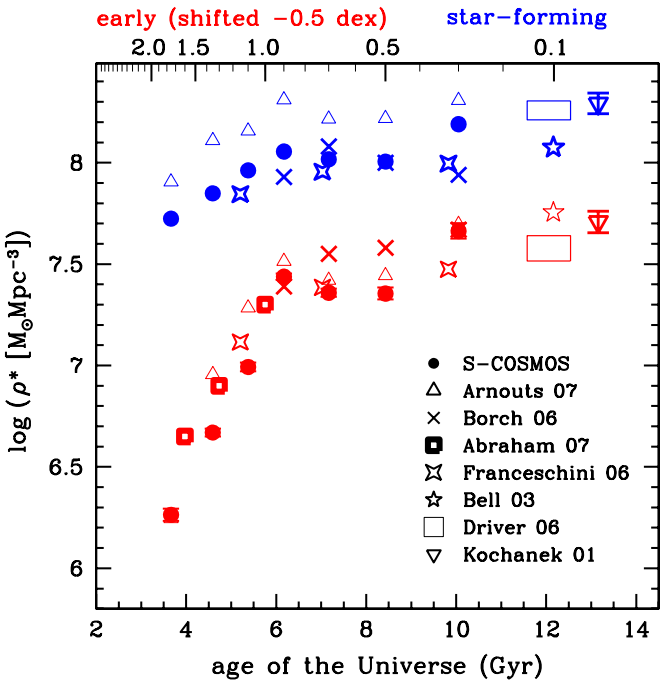

Figure 24. Evolution of the stellar mass density of star-forming (blue filled circles) and quiescent galaxies (red filled circles) compared to various results from the literature. The stellar mass density of all the red sequence and quiescent galaxies is shifted vertically by −0.5 dex for the clarity of the figure. The offset of 0.2 dex between Arnouts et al. (2007) and our measurement for star-forming galaxies is discussed in Appendix D.

(A color version of this figure is available in the online journal.)

9.3. Slow Down in the Assembly of Massive Quiescent Galaxies at $z \sim 1$

The most massive quiescent galaxies are not in place at $z \sim 2$ and their number density evolves rapidly between $z \sim 2$ and $z \sim 1$. The exponential cutoff of their MF increases by 0.4 dex between $z = 1.5$–2 and $z = 0.8$–1. Figure 24 shows that the rapid assembly rate of quiescent galaxies at $1 < z < 2$ is consistent with other surveys, despite the different methods used to classify early-type galaxies, to determine the stellar masses, and to measure the distances (spectro-z or photo-z). Using deeper data in the GOODS field, we also checked that our results do not suffer from a significant incompleteness which could mimic the rapid assembly of quiescent galaxies at $1 < z < 2$ (see Appendix E).

Therefore, the most massive quiescent galaxies are created rapidly between $z \sim 2$ and $z \sim 1$ and their assembly slows down at $z < 1$. We tentatively explain this slow down in their evolution by analyzing the relative evolution of the quiescent and star-forming MFs from $z = 2$ to $z = 0.2$.

Figure 25 shows the fraction of quiescent galaxies as a function of stellar mass. The quiescent galaxies represent less than 20% of the most massive galaxies at $z = 1.5$–2. As a consequence, "wet mergers" between massive star-forming galaxies directly create new massive quiescent galaxies (since star-forming galaxies are more massive and more numerous) which generates a rapid growth of the quiescent high-mass end between $z \sim 2$ and $z \sim 1$.

[20] Bekki (2008) simulated merging between gas rich spiral galaxies of mass $\mathcal{M} \sim 10^9\ \mathcal{M}_\odot$, which formed a dynamically relaxed low mass elliptical galaxy in 1.4 Gyr with a SFR of 0.03 $M_\odot\ \mathrm{yr}^{-1}$.

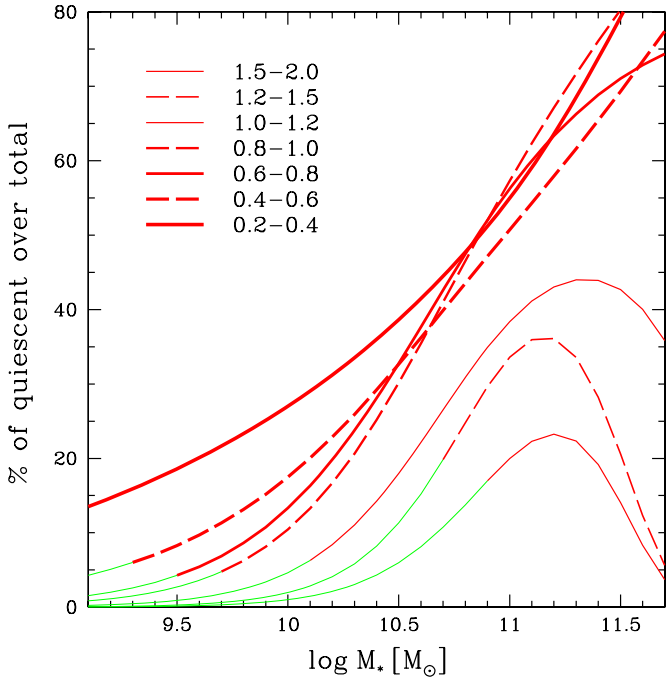

Figure 25. Fraction of the "quiescent" over the total population per stellar mass bin (MF of the quiescent divided by the total MF). The thick red line corresponds to the stellar mass range covered by the data. The thin green line is obtained using the extrapolation of the MF with the Schechter function.

(A color version of this figure is available in the online journal.)

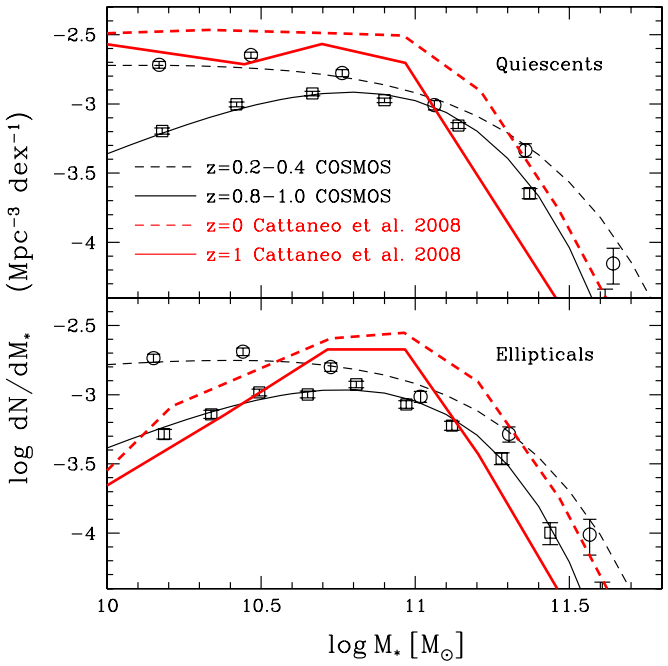

Figure 26. MF of "quiescent" galaxies (thick red lines in the top panel) and elliptical galaxies (thick red lines in the bottom panel) at $z = 0$ and $z = 1$ predicted by Cattaneo et al. (2008) using the GalICS semi-analytical simulations and a "halo quenching" model. Our quiescent and red elliptical MFs are reported in each panel.

(A color version of this figure is available in the online journal.)

A change of regime occurs at $z < 1$, where the exponential cutoff of star-forming galaxies is shifted at lower mass than the exponential cutoff of quiescent galaxies (see Figure 17). This change is likely explained by the rapid increase of the massive quiescent population at $1 < z < 2$, combined with the decrease of the SFR at $z < 1$ (e.g., Lilly et al. 1996; Le Floc'h et al. 2005; Tresse et al. 2007) which prevents to regenerate the massive star-forming population. Therefore, the quiescent population dominates the massive end of the MF at $z < 1$, with more than 60%–70% of quiescent galaxies at $\log \mathcal{M} > 11$–11.5. As a consequence, "wet mergers" become inefficient at $z < 1$ to generate the most massive quiescent galaxies.

Dry merging (merging between quiescent galaxies, e.g., Van Dokkum & Franx 2001) is the only process left to form the most massive quiescent galaxies at $z < 1$. This process has less impact on the quiescent MF evolution since "dry merging" is not a direct supply of new quiescent systems (the progenitors are already quiescent galaxies). Moreover, "dry merging" involving two massive quiescent galaxies ($\log \mathcal{M} > 11$) is not a common process since the exponential cutoff of the quiescent MF does not evolve significantly at $z < 1$.

Therefore, the disappearance of "wet merging" as an efficient process to form the most massive ellipticals could explain the slow down in their assembly at $z < 1$.

9.4. Indirect Constraints on the AGN Feedback

Two different modes of AGN activity are usually considered: the "bright mode" (e.g., QSO) and the "radio mode" which radiates less energy than the "bright mode" but is a more common mechanism (e.g., Croton et al. 2006). In both modes, the AGN feedback can prevent the gas to cool in the dark matter halo. Since the "radio mode" is less energetic, the radio jet from the black hole prevent the gas to cool only in quasi-hydrostatic shock-heated halos, i.e., in halos above a critical mass around 10^{12} $M_\odot$ (Cattaneo et al. 2006; Somerville et al. 2008).

As a consequence, the radio mode prevents the star formation of recurring in all the galaxies of massive halos. Therefore, the star formation is shut down in the galaxy hosting the AGN, but also in all the galaxies surrounding the AGN. We discuss here the impact of AGN feedback on the "surrounding galaxies."[21] A specific study on the host galaxies of the radio sources is presented in Smolčić et al. (2009).

The shutdown of the star formation in the "surrounding galaxies" does not modify their morphology. As their original morphology can be any, we then expect a significant population of quiescent galaxies with a Spi/Irr morphology. Indeed, the ratio between the red elliptical and the quiescent MFs shows a significant fraction of Spi/Irr having a quenched star formation at low masses (40%–60% at $\log \mathcal{M} \sim 9.5$; see Figure 14), which leaves room for this "external" action mode of AGN feedback.

More quantitatively, Cattaneo et al. (2008) provided the predicted MFs for quiescent (red sequence in Cattaneo et al.) and elliptical (bulge-dominated in Cattaneo et al.) galaxies at $z = 0$ and $z = 1$. They used a "halo quenching" model (Somerville et al. 2008). In this model, the AGN feedback shuts down the star formation in all the galaxies within a halo more massive than 10^{12} $M_\odot$ (Cattaneo et al. 2006; Somerville et al. 2008). We report in Figure 26 the MF predicted by Cattaneo et al. (2008). As expected, the predicted density of quiescent galaxies stays constant at low/intermediate masses (top panel), while the density of elliptical galaxies decreases toward low masses (bottom panel). On the basis of these predicted MFs, ∼10% of

[21] We call "surrounding galaxies" the galaxies which belong to the same halo as the AGN but which are not hosting the AGN themselves. These galaxies are satellite galaxies if the AGN is hosted by the central galaxy of the dark matter halo.

the quiescent galaxies would be elliptical at $\log \mathcal{M} \sim 10$. By contrast, we found a fraction of 80% (60%) quiescent galaxies with an elliptical morphology (see Figure 14). Therefore, quenched star formation is more often linked to an elliptical morphology than would be predicted by a "halo quenching" model. These measurements constrain in the same way all the processes quenching star formation without modifying the galaxy morphology, for example, gas starvation (i.e., satellite galaxies not fueled in cold gas since they are not at the center of the dark matter halo potential well).

A more quantitative constraint on these mechanisms requires a detailed comparison with predictions of semi-analytical simulations, which is planned for forthcoming papers.

10. CONCLUSION

We derived the galaxy stellar MF and stellar mass density in the 2 deg^2 COSMOS field. We explored stellar mass assembly by morphological and spectral type from $z = 2$ to $z = 0.2$. The MF estimate is based on 196,000 galaxies selected at $F_{3.6\,\mu\mathrm{m}} > 1\,\mu$Jy and photo-$z$ with an accuracy of $\sigma_{(z_{\mathrm{phot}}-z_{\mathrm{spec}})/(1+z_{\mathrm{spec}})} = 0.008$ at $i^+_{\mathrm{AB}} > 22.5$. We summarize our results below.

1. We found that $z \sim 1$ is an epoch of transition in the assembly of quiescent galaxies. Their stellar mass density increases by 1.1 dex between $z = 1.5$–2 and $z = 0.8$–1 (corresponding to a period of 2.5 Gyr), but only by 0.3 dex between $z = 0.8$–1 and $z \sim 0.1$ (a period of 6 Gyr). The high-mass exponential cutoff of the quiescent MF increases by 0.4 dex between $z = 1.5$–2 and $z = 0.8$–1, but almost no evolution is seen at $z < 1$. We investigated if the weak evolution of the most massive quiescent galaxies is also seen using a morphological classification. The exponential cutoff of massive red elliptical galaxies does not increase significantly at $z < 1$. Moreover, the blue elliptical galaxies do not contribute more than 20% to the high-mass end of the total elliptical sample, which is not sufficient to produce significant evolution in the exponential cutoff.
2. We found that the high-mass end of the star-forming MF is shifted below the high-mass end of the quiescent MF at $z < 1$. Therefore, we interpreted the slow down in the assembly of the most massive elliptical galaxies at $z < 1$ as being due to a "lack of supply" of massive star-forming galaxies available for "wet mergers."
3. We observed a rapid rise of quiescent galaxies at low/intermediate masses. We characterized the nature of these newly formed quiescent galaxies by adding morphological information. We quantified the fraction of quiescent galaxies with an elliptical morphology, as well as the fraction of Spi/Irr galaxies with quenched star formation. The significant fraction of quenched Spi/Irr (40%–60% at $\log \mathcal{M} \sim 9.5$) leaves room for a mechanism which shuts down the star formation without transforming their morphology, such as the impact of AGN feedback on the satellite galaxies of a massive halo (e.g., Cattaneo et al. 2006). Since the majority of quiescent galaxies have an elliptical morphology at $z < 0.8$ (80%–90% at $\log \mathcal{M} \sim 11$), the dominant process which shuts down star formation should be linked to the acquisition of an elliptical morphology, as might be expected in galaxy merging and/or morphological quenching (Martig et al. 2009).
4. Finally, we divided the star-forming sample into "intermediate activity" and "high activity" galaxies, which corresponds to two classes of SSFR (SFR divided by stellar mass). The MF of the "high activity" galaxies shows that the most massive of them end their high activity phase first. Therefore, the low mass star-forming galaxies are able to maintain a high SSFR, while the massive galaxies evolve rapidly into systems with a lower SSFR. This redistribution of the star formation activity follows a clear "downsizing" pattern (Cowie et al. 1996) within the star-forming sample itself.

We are grateful to the referee for his/her careful reading of the manuscript and his/her useful suggestions.

This work is based on observations made with the *Spitzer Space Telescope*, which is operated by the Jet Propulsion Laboratory, California Institute of Technology under NASA contract 1407. Support for this work was provided by NASA through Contract Number 1278386 issued by JPL. We gratefully acknowledge the contributions of the entire COSMOS collaboration consisting of more than 100 scientists. The *HST* COSMOS program was supported through NASA grant HST-GO-09822. More information on the COSMOS survey is available at http://www.astro.caltech.edu/cosmos.

APPENDIX A

ABSOLUTE MAGNITUDE ESTIMATE

At high redshift, the k-correction is one of the main sources of systematic error in the absolute magnitude and rest-frame color estimate. The k-correction depends on the galaxy SED, which is not directly observed (Oke & Sandage 1968). In order to minimize the uncertainty induced by the k-correction term, the rest-frame luminosity at a given wavelength, λ, is derived from the apparent magnitude observed at $\lambda \times (1 + z)$ (Appendix A of Ilbert et al. 2005). With this procedure, the absolute magnitudes are less dependent on the SED. One drawback of this method is that the uncertainty in the observed apparent magnitude is directly propagated into the absolute magnitude. For this reason, the absolute magnitudes were measured from one of the following bands $u^* g^+ r^+ i^+ z^+ K$ and 3.6 μm all of which have the highest signal-to-noise ratio and a zero-point correction lower than 0.05 mag (Ilbert et al. 2009).

APPENDIX B

ADDITIONAL CONSTRAINT IN THE TEMPLATE-FITTING USING THE 24 μm FLUXES

The deep MIPS S-COSMOS data were taken during Spitzer Cycle 3 and cover the full COSMOS 2 deg^2 (H. Aussel et al. 2010, in preparation). The 24 μm sources were detected with SExtractor (Bertin & Arnouts 1996) and their fluxes measured with a PSF fitting technique (Le Floc'h et al. 2009). The infrared luminosities $L_{\mathrm{IR}}^{\mathrm{MIPS}}$ were extrapolated from the 24 μm fluxes using the Dale & Helou (2002) library (Le Floc'h et al. 2009) and converted into $\mathrm{SFR_{IR}}$ using the calibration from Kennicutt (1998).

The stellar mass estimate and instantaneous SFR (hereafter $\mathrm{SFR_{template}}$) are derived from the best-fit template. We compared $\mathrm{SFR_{template}}$ and $\mathrm{SFR_{IR}}$ in order to decide which extinction law to adopt—either Calzetti et al. (2000) or Charlot & Fall (2000). Figure 27 shows that the use of the Calzetti et al. (2000) extinction law reduces the systematic offset between $\mathrm{SFR_{template}}$ and $\mathrm{SFR_{IR}}$. Therefore, we favored the Calzetti et al. extinction law for our analysis.

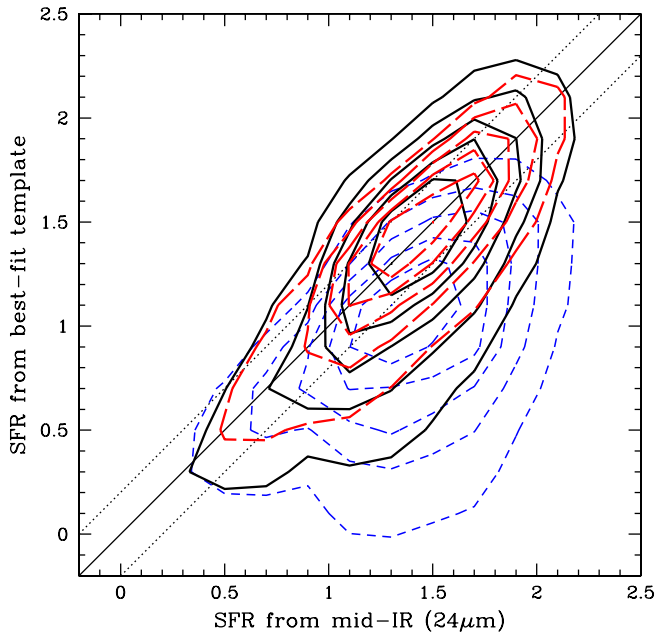

Figure 27. SFR estimated from the best-fit template vs. the SFR directly measured using the mid-infrared 24 μm MIPS flux. The short-dashed blue contours and solid black contours are obtained using the Charlot & Fall (2000) extinction law and the Calzetti et al. (2000) extinction laws, respectively. The long-dashed red contours are obtained using the constraint on the 24 μm flux.

(A color version of this figure is available in the online journal.)

As a second step, we used the 24 μm MIPS fluxes as an additional constraint in the template-fitting procedure. The goal of this additional constraint is to remove possible degeneracies between "old and quiescent" models and "star-forming and dust-extincted" models. For each template, we computed $L_{\rm IR}^{\rm template}$, which is the infrared luminosity which would be re-emitted in the infrared according to the template, assuming that all of the UV light absorbed by dust is re-emitted in the infrared and that the massive stars are the only source of infrared emission. A likelihood, $\mathcal{L}$, is computed at each step of the template-fitting procedure. We multiplied this likelihood by the probability to measure $L_{\rm IR}^{\rm MIPS}$ for a given template:

$$\mathcal{L}' \propto \mathcal{L}(\text{template, scaling, } E(B-V)) \frac{\exp\left(-\frac{\left(L_{\rm IR}^{\rm MIPS}-L_{\rm IR}^{\rm template}\right)^2}{2\times \text{err}^2}\right)}{\text{err}\times\sqrt{2\pi}}, \quad \text{(B1)}$$

where err is the error on the $L_{\rm IR}^{\rm MIPS}$ measurement (Le Floc'h et al. 2009). We added 0.2 dex in quadrature to the error on $L_{\rm IR}^{\rm MIPS}$ to take into account systematic uncertainties in $L_{\rm IR}^{\rm MIPS}$. When the galaxy has no MIPS counterpart at more than 2″, an upper limit is applied to the $L_{\rm IR}^{\rm template}$. This upper limit corresponds to the lowest $L_{\rm IR}^{\rm MIPS}$ observable for a sample selected at $F_{24\,\mu\rm m} > 100\,\mu$Jy ($5\sigma$ completeness limit). No prior is applied if the optical counterpart is between 0.″6 and 2″ (less secure optical counterpart).

By construction, the comparison between $\rm SFR_{template}$ and $\rm SFR_{IR}$ is improved by this prior as shown in Figure 27.

APPENDIX C

THE TOOL ALF

The selection of the galaxy sample at $F_{3.6\,\mu\rm m} > 1\,\mu$Jy defines a limit in redshift above which the galaxies are too faint to be observed. Statistical estimators are required to correct for the incompleteness created by this flux limit.

We measured the luminosity and stellar MFs using the tool ALF described in Ilbert et al. (2005) and originally developed to measure the luminosity functions from the VIMOS-VLT Deep Survey (Le Fèvre et al. 2005). The procedures used to compute the stellar MF or the luminosity function are the same. The tool includes various estimators: the non-parametric $1/V_{\rm max}$, C^+, SWML, and the parametric STY. The STY (Sandage et al. 1979) and SWML (Efstathiou et al. 1988) determine the MF by maximizing the likelihood to observe a given stellar mass-redshift sample. The STY estimator presupposes that the MF can be parameterized with a Schechter function (Schechter 1976):

$$\Phi(M)dM = \Phi^*(M/M^*)^\alpha \ \exp(-M/M^*)\ d(M/M^*). \quad \text{(C1)}$$

This parameterization allows us to describe the MF using three parameters: α (slope), $\mathcal{M}^*$ (characteristic stellar mass), and ϕ^* (normalization). The SWML is a non-parametric estimate of the MF, useful to verify that a Schechter function is a good representation of the data. The non-parametric $1/V_{\rm max}$ estimator (Schmidt 1968) is the most widely used because of its simplicity. The $1/V_{\rm max}$ is the inverse sum of the volume in which each galaxy could be observed. The $1/V_{\rm max}$ is the only estimator directly normalized. Lynden-Bell (1971) derived the non-parametric C^- method to overcome the assumption of a uniform galaxy distribution derived using $1/V_{\rm max}$ (we used a slightly modified version called C^+; Zucca et al. 1997). The implementation of these estimators is detailed in Appendix A of Ilbert et al. (2005).

APPENDIX D

MASS-TO-LIGHT RATIO

The K-band luminosity is not a direct tracer of the stellar mass. Numerous analyses have used an analytical parameterization of the mass-to-light ratio in order to derive the stellar masses (e.g., Kochanek et al. 2001; Driver et al. 2007; Arnouts et al. 2007).

The left panel of Figure 28 shows the mass-to-light ratio as a function of redshift (the stellar masses are derived as described in Section 4.1). We observed a decrease of the mass-to-light ratio with redshift, in good agreement with the empirical relations derived by Arnouts et al. (2007). We also found that the mass-to-light ratio increases with the stellar mass. This trend is expected since the high-mass galaxies are older and have a larger mass-to-light ratio. The right panel of Figure 28 shows the difference between the observed mass-to-light ratio and the analytical relation derived by Arnouts et al. (2007). For the quiescent galaxies, the median difference is below 0.1 dex. The median difference is also below 0.1 dex for the star-forming galaxies ($\log\mathcal{M} > 10.5$), but the median difference is shifted below −0.3 dex at low masses $\log\mathcal{M} < 9.5$, showing that this relation is not anymore a good proxy for the low-mass galaxies.

We compared our stellar mass densities for star-forming galaxies with results from the literature in Figure 24. The stellar mass densities of Arnouts et al. (2007) are systematically 0.2 dex higher than our measurements. Arnouts et al. (2007) based their measurements on the K-band LF converted into stellar mass density using the mass-to-light relation discussed above. At low masses ($\log\mathcal{M} < 10$), we found mass-to-light ratio lower by 0.2–0.4 dex than those estimated from the Arnouts et al. (2007) relation. Since star-forming galaxies are mostly low/intermediate mass galaxies (steep slope of their MF), the

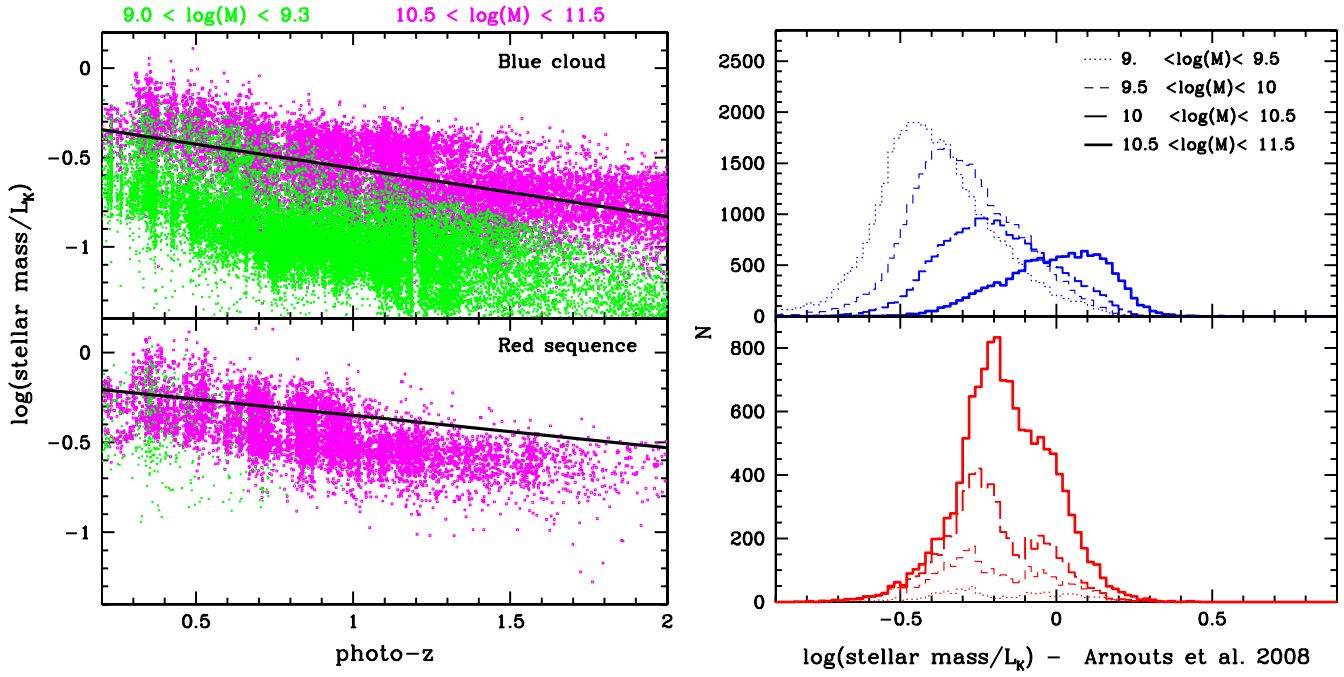

Figure 28. Left panels: mass-to-light ratio as a function of redshift. The stellar masses are computed from a SED fitting procedure. The luminosity is measured in the rest-frame K_s band. The top and bottom panels correspond to the blue cloud and red sequence galaxies, respectively. The solid lines correspond to the empirical relations derived by Arnouts et al. (2007). The relation of Arnouts et al. (2007) is derived for the massive galaxies brighter than $m_{3.6\,\mu m} < 21.5$. The magenta crosses and the green circles are the galaxies selected in stellar mass ranges $9.0 < \log \mathcal{M} < 9.5$ and $10.5 < \log \mathcal{M} < 11.5$, respectively. Right panels: difference between the observed mass-to-light ratio and the analytical relation established by Arnouts et al. (2007). The top and bottom panels correspond to the star-forming and quiescent galaxies, respectively. The difference is shown per bin of stellar mass.

(A color version of this figure is available in the online journal.)

dependency of the mass-to-light ratio on the mass likely explains this offset of 0.2 dex in the stellar mass densities.

APPENDIX E

THE QUIESCENT MFs IN THE GOODS AND COSMOS FIELDS

Two possible sources of incompleteness could affect our estimate of the quiescent MFs at $z > 1$: the depth of the optical catalog and the confusion in the IRAC images. We checked the validity of our selection criteria using the GOODS data sets (Giavalisco et al. 2004). We used the public catalogs FIREWORKS (Wuyts et al. 2008) and MUSIC (Santini et al. 2009). The IRAC photometry in these catalogs is less affected by the confusion since specific softwares allow an accurate "PSF-matching" (e.g., CONVPHOT in Santini et al. 2009). The GOODS optical data are also deeper than COSMOS (90% complete in ACS/F775W at 26.5 mag).

We selected the FIREWORKS and MUSIC catalogs at $F(3.6\,\mu m) > 1\,\mu$Jy, which is the selection limit of our study. We computed the photo-z using the code "Le Phare" and the same setting (templates, extinction,...) as Ilbert et al. (2009). The rest-frame colors and stellar masses were estimated following exactly the method described in Section 4.3. We also classified galaxies according to their dust-corrected NUV $-$ R rest-frame colors as in Section 3.2.

First, we find that the contribution of galaxies fainter than $I = 26.5$ is negligible at the considered stellar mass limits (see Table 2). Then, we derive the quiescent MFs in GOODS (using both MUSIC and FIREWORKS catalogs, as well as their original photo-z). The comparison with the S-COSMOS MFs is shown in Figure 29. The results are in excellent agreement. The

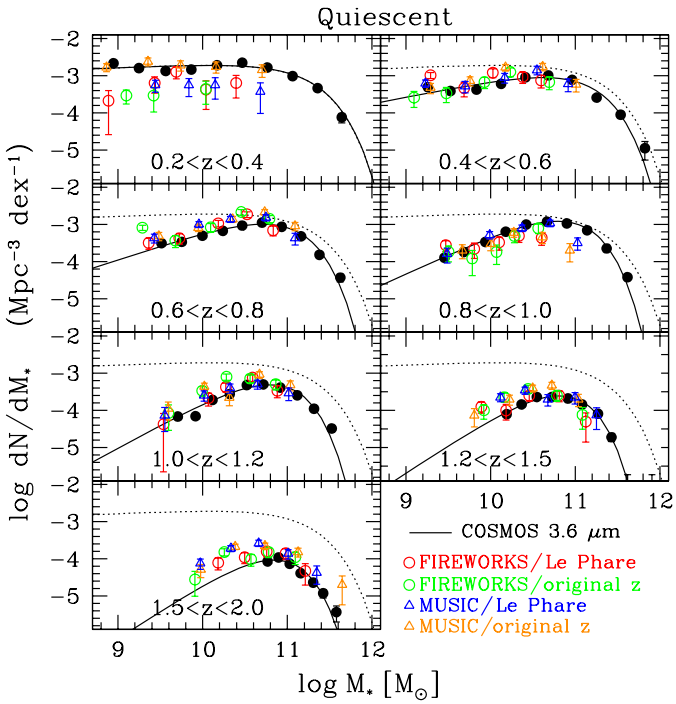

Figure 29. Stellar mass functions of the quiescent population in the GOODS and COSMOS fields. The black filled circles correspond to the S-COSMOS estimate of the quiescent MFs. The open points are the quiescent MFs measured in the GOODS field. Red and green circles are an estimate based on the FIREWORKS catalog using "Le Phare" and the Wuyts et al. (2008) photo-z, respectively. Blue and orange triangles are an estimate based on the MUSIC catalog using "Le Phare" and the Santini et al. (2009) photo-z, respectively.

(A color version of this figure is available in the online journal.)

differences could be easily explained by cosmic variance since the GOODS field covers only 160 arcmin^2. The only significant difference is seen using the GOODS-MUSIC catalog and their own set of photo-z at $z > 1.2$ (a factor $\sim$1.5 in normalization). From this comparison, we conclude that our results do not suffer from any significant incompleteness at $z > 1$ and that the rapid assembly of the quiescent population at $1 < z < 2$ cannot be explained by incompleteness or confusion effects.

REFERENCES

Abraham, R. G., Invar, N. R., Santiago, B. X., Ellis, R. S., Glazebrook, K., & van den Bergh, S. 1996, MNRAS, 279, L47
Abraham, R. G., et al. 2007, ApJ, 669, 184
Arnouts, S., et al. 2002, MNRAS, 329, 355
Arnouts, S., et al. 2007, A&A, 476, 137
Athanassoula, E. 2008, MNRAS, 390, 69
Bekki, K. 2008, MNRAS, 388, L10
Bell, E. F. 2008, ApJ, 682, 355
Bell, E. F., McIntosh, D. H., Katz, N., & Weinberg, M. D. 2003, ApJS, 149, 289
Bell, E. F., et al. 2004, ApJ, 608, 752
Benson, A. J., Bower, R. G., Frenk, C. S., Lacey, C. G., Baugh, C. M., & Cole, S. 2003, ApJ, 599, 38
Bertin, E., & Arnouts, S. 1996, A&AS, 117, 393
Boissier, S., Buat, V., & Ilbert, O. 2009, A&A, submitted
Borch, A., et al. 2006, A&A, 453, 869
Bower, R. G., Benson, A. J., Malbon, R., Helly, J. C., Frenk, C. S., Baugh, C. M., Cole, S., & Lacey, C. G. 2006, MNRAS, 370, 645
Brusa, M., et al. 2007, ApJS, 172, 353
Bruzual, G. A. 2007, in ASP Conf. Ser. 374, From Stars to Galaxies: Building the Pieces to Build Up the Universe, ed. A. Vallenari et al. (San Francisco, CA: ASP), 303
Bruzual, G., & Charlot, S. 2003, MNRAS, 344, 1000 (BC03)
Bundy, K., Ellis, R. S., & Conselice, C. J. 2005, ApJ, 625, 621
Bundy, K., et al. 2006, ApJ, 651, 120
Bundy, K., et al. 2009, ApJ, submitted
Calzetti, D., et al. 2000, ApJ, 533, 682
Capak, P., Abraham, R. G., Ellis, R. S., Mobasher, B., Scoville, N., Sheth, K., & Koekemoer, A. 2007, ApJS, 172, 284
Cassata, P., et al. 2007, ApJS, 172, 270
Cattaneo, A., Dekel, A., Devriendt, J., Guiderdoni, B., & Blaizot, J. 2006, MNRAS, 370, 1651
Cattaneo, A., Dekel, A., Faber, S. M., & Guiderdoni, B. 2008, MNRAS, 389, 567
Chabrier, G. 2003, PASP, 115, 763
Charlot, S., & Fall, S. M. 2000, ApJ, 539, 718
Cimatti, A., Daddi, E., & Renzini, A. 2006, A&A, 453, L29
Cirasuolo, M., et al. 2007, MNRAS, 380, 585
Cowie, L. L., & Barger, A. J. 2008, ApJ, 697, 122
Cowie, L. L., Songaila, A., Hu, E. M., & Cohen, J. G. 1996, AJ, 112, 839
Cross, N. J. G., et al. 2004, AJ, 128, 1990
Croton, D. J., et al. 2006, MNRAS, 365, 11
Dale, D. A., & Helou, G. 2002, ApJ, 576, 159
De Lucia, G., Springel, V., White, S. D. M., Croton, D., & Kauffmann, G. 2006, MNRAS, 366, 499
De Ravel, L., et al. 2009, A&A, 498, 379
de Santis, C., Grazian, A., Fontana, A., & Santini, P. 2007, New Astron., 12, 271
Driver, S. P., Allen, P. D., Liske, J., & Graham, A. W. 2007, ApJ, 657, L85
Drory, N., et al. 2009, ApJ, 707, 1595
Efstathiou, G., Ellis, R. S., & Peterson, B. A. 1988, MNRAS, 232, 431
Faber, S. M., et al. 2007, ApJ, 665, 265
Fioc, M., & Rocca-Volmerange, B. 1997, A&A, 326, 950
Fontana, A., et al. 2004, A&A, 424, 23
Fontana, A., et al. 2006, A&A, 459, 745
Franceschini, A., et al. 2006, A&A, 453, 397
Franzetti, P., et al. 2007, A&A, 465, 711
Giavalisco, M., et al. 2004, ApJ, 600, L93
Hammer, F., Puech, M., Chemin, L., Flores, H., & Lehnert, M. D. 2007, ApJ, 662, 322
Hasinger, G., et al. 2007, ApJS, 172, 29
Ilbert, O., et al. 2004, MNRAS, 351, 541
Ilbert, O., et al. 2005, A&A, 439, 863
Ilbert, O., et al. 2006a, A&A, 453, 809
Ilbert, O., et al. 2006b, A&A, 457, 841
Ilbert, O., et al. 2009, A&A, 690, 1236
Kartaltepe, J. S., et al. 2007, ApJS, 172, 320
Kauffmann, G., White, S. D. M., & Guiderdoni, B. 1993, MNRAS, 264, 201
Kennicutt, R. C. 1998, ARA&A, 36, 189
Kereš, D., Katz, N., Weinberg, D. H., & Davé, R. 2005, MNRAS, 363, 2
Kitzbichler, M. G., & White, S. D. M. 2007, MNRAS, 376, 2
Kochanek, C. S., et al. 2001, ApJ, 560, 566
Koekemoer, A. M., et al. 2007, ApJS, 172, 196
Laidler, V. G., et al. 2007, PASP, 119, 1325
Lauger, S., Burgarella, D., & Buat, V. 2005, A&A, 434, 73
Le Fèvre, O., et al. 2000, MNRAS, 311, 565
Le Fèvre, O., et al. 2005, A&A, 439, 845
Le Floc'h, E., et al. 2005, ApJ, 632, 169
Le Floc'h, E., et al. 2009, ApJ, 703, 222
Lilly, S. J., Le Fèvre, O., Hammer, F., & Crampton, D. 1996, ApJ, 460, L1
Lin, H., Yee, H. K. C., Carlberg, R. G., Morris, S. L., Sawicki, M., Patton, D. R., Wirth, G., & Shepherd, C. W. 1999, ApJ, 518, 533
Longhetti, M., & Saracco, P. 2008, MNRAS, 394, 774
Lotz, J. M., Primack, J., & Madau, P. 2004, AJ, 128, 163
Lotz, J. M., et al. 2008, ApJ, 672, 177
Lynden-Bell, D. 1971, MNRAS, 155, 95
Maraston, C. 2005, MNRAS, 362, 799
Martig, M., Bournaud, F., Teyssier, R., & Dekel, A. 2009, ApJ, 707, 250
Martin, D. C., et al. 2007, ApJS, 173, 342
McCracken, H. J., et al. 2010, ApJ, 708, 202
Menanteau, F., Ford, H. C., Motta, V., Benitez, N., Martel, A. R., Blakeslee, J. P., & Infante, L. 2006, AJ, 131, 208
Menci, N., Fontana, A., Giallongo, E., Grazian, A., & Salimbeni, S. 2006, ApJ, 647, 753
Oesch, P., et al. 2009, ApJ (arXiv:0911.1126)
Oke, J. B., & Sandage, A. 1968, ApJ, 154, 21
Pannella, M., Hopp, U., Saglia, R. P., Bender, R., Drory, N., Salvato, M., Gabasch, A., & Feulner, G. 2006, ApJ, 639, L1
Pozzetti, L., et al. 2007, A&A, 474, 443
Pozzetti, L., et al. 2009, A&A, submitted (arXiv:0907.5416)
Rettura, A., et al. 2006, A&A, 458, 717
Salvato, M., et al. 2009, ApJ, 690, 1250
Sandage, A., Tammann, G. A., & Yahil, A. 1979, ApJ, 232, 352
Sanders, D. B., et al. 2007, ApJS, 172, 86
Santini, P., et al. 2009, A&A, 504, 751
Scarlata, C., et al. 2007, ApJS, 172, 494
Schechter, P. 1976, ApJ, 203, 297
Schmidt, M. 1968, ApJ, 151, 393
Scoville, N., et al. 2007, ApJS, 172, 1
Smolčić, V., et al. 2009, ApJ, 696, 24
Somerville, R. S., Hopkins, P. F., Cox, T. J., Robertson, B. E., & Hernquist, L. 2008, MNRAS, 391, 481
Springel, V., Frenk, C. S., & White, S. D. M. 2006, Nature, 440, 1137
Strateva, I., et al. 2001, AJ, 122, 1861
Stringer, M. J., Benson, A. J., Bundy, K., Ellis, R. S., & Quetin, E. L. 2009, MNRAS, 393, 1127
Surace, J. A., Shupe, D. L., Fang, F., Evans, T., Alexov, A., Frayer, D., Lonsdale, C. J. M., & SWIRE Team 2005, BAAS, 37, 1246
Takeuchi, T. T., Buat, V., & Burgarella, D. 2005, A&A, 440, L17
Toomre, A., & Toomre, J. 1972, ApJ, 178, 623
Tresse, L., et al. 2007, A&A, 472, 403
Van Dokkum, P. G., & Franx, M. 2001, ApJ, 553, 90
Vergani, D., et al. 2008, A&A, 487, 89
White, S. D. M., & Rees, M. J. 1978, MNRAS, 183, 341
Williams, R. J., et al. 2009, ApJ, 691, 1879
Wolf, C., Meisenheimer, K., Rix, H.-W., Borch, A., Dye, S., & Kleinheinrich, M. 2003, A&A, 401, 73
Wuyts, S., Labbé, I., Schreiber, N. M. F., Franx, M., Rudnick, G., Brammer, G. B., & van Dokkum, P. G. 2008, ApJ, 682, 985
Zucca, E., et al. 1997, A&A, 326, 477
Zucca, E., et al. 2006, A&A, 455, 879